Computers and Structures 184 (2017) 36–52

Contents lists available at ScienceDirect

Computers and Structures

journal homepage: www.elsevier.com/locate/compstruc

Meshfree analysis of electromagnetic wave scattering from conducting targets: Formulation and computations

W.L. Nicomedes [a,*], K.J. Bathe [b], F.J.S. Moreira [c], R.C. Mesquita [d]

[a] Graduate Program in Electrical Engineering, Federal University of Minas Gerais, Belo Horizonte MG 31270-901, Brazil
[b] Dept. Mechanical Engineering, Massachusetts Institute of Technology, Cambridge, MA 02139, USA
[c] Dept. Electronics Engineering, Federal University of Minas Gerais, Brazil
[d] Dept. Electrical Engineering, Federal University of Minas Gerais, Brazil

ARTICLE INFO

Article history:
Received 13 November 2016
Accepted 27 January 2017
Available online 6 March 2017

Keywords:
Electromagnetics
Finite elements
Inf-sup condition
Meshfree methods
Mixed/hybrid formulations
Wave scattering

ABSTRACT

We propose a completely meshfree procedure aimed at the time-harmonic analysis of electromagnetic wave scattering from conducting targets. The problem is described by the vector wave equation with a divergence-free constraint. We propose a mixed formulation whose unknowns are the electric field vector and a Lagrange multiplier. We investigate the well-posedness of the variational problem and construct compatible meshfree function spaces able to describe solutions in any geometry, in two and three dimensions. The method does not depend on any kind of parameter tuning. We illustrate its performance in a number of solutions through experimentally derived convergence rates and comparisons with other techniques.

1. Introduction

Meshfree (or meshless) methods refer to a broad category of numerical procedures applied to the solution of differential equations. In some cases, the methods can be interpreted as a generalization of finite element methods [1–5]. The applications in research using meshfree methods are numerous, following the publication of some papers introducing these methods in computational mechanics, like the Smooth Particle Hydrodynamics (SPH) method [6], the Element Free Galerkin (EFG) method [7], the Local Boundary Integral Equation (LBIE) method [8,9], the Finite Spheres method [10,11], and the Meshless Local Petrov-Galerkin (MLPG) method [12].

Specific meshfree methods can be quite different from others. Features like the imposition of boundary conditions and the construction of interpolation functions, for example, are dealt with very differently depending on the method. However, there is one characteristic that is common to all meshfree methods: They rely on *nodes* scattered freely throughout the computational domain. There is no mesh or grid connecting these nodes. Indeed, it is one of the aims in the development of meshfree methods to circumvent the difficulties associated with the generation of a mesh, particularly in three dimensions. In some cases the methods construct independent basis functions defined on small regions around the nodes, called *subdomains*, *spheres*, or *patches*. These and generalizations thereof have recently been labeled 'overlapping finite elements' because the overlapping is the main characteristic distinguishing them from traditional finite elements [1,2]. The computational domain is covered by these overlapping elements. Comprehensive studies of meshfree methods in the solution of problems in mechanics led to the current research in applications of ever-increasing levels of complexity [13–21].

In electromagnetics, the introduction of meshfree methods as an alternative to the use of finite element methods came a few years later [22–25]. Some research in this field is focused on *collocation* procedures, i.e., methods which deal with the differential equations in *strong form*. They usually use Radial Point Interpolation (RPIM) basis functions, and can be seen as suitable alternatives to finite difference methods [26–28]. While simpler to implement, these methods suffer from instabilities or may not be fully meshfree [29].

Meshfree methods based on *weak forms* have also been considered. Some research has been focused on the EFG method [30–33], but because the EFG method relies on background cells to perform the numerical integrations, it is not considered a truly meshfree method. On the other hand the MLPG method is a truly meshfree procedure and has been used in electromagnetics, see for example [34–36].

* Corresponding author.
E-mail address: wnicomedes@eng-ele.grad.ufmg.br (W.L. Nicomedes).

http://dx.doi.org/10.1016/j.compstruc.2017.01.014
0045-7949/

It is by now an established fact that meshfree methods based on weak forms can be used in electrical engineering, see also [37–39]. However, all the solution examples in [30–39] deal with *scalar field* problems. The extension of meshfree procedures based on variational forms to *vector field problems* in $\mathbb{R}^d$ ($d = 2$ or 3) is a significant step due to the difficulty in satisfying the divergence-free condition, and only few research efforts have been published, see for example [40]. Using finite element methods, vector field problems in electromagnetics are usually solved employing Nédélec edge elements [41–44]. In this approach, degrees of freedom are associated with each edge in the mesh (generally formed by, but not restricted to, triangles in 2D and tetrahedra in 3D), and the resulting basis functions are such that their divergence is zero within each element (but not at the element boundaries) [43].

In a true meshfree setting, we do not have the support of a mesh, which poses some difficulty in constructing appropriate vector basis functions. Some results using a meshfree procedure based on weak forms in the solution of vector electromagnetic field problems are for example given in [40]. The strategy in that work is to define vector basis functions on the patches. Despite the success, there are at least three points that deserve attention. First, the method has not been tested on curvilinear geometries. Second, the imposition of essential boundary conditions is based on Nitsche's method [45], in which the formulation incorporates to the weak forms extra regularization terms that depend on adjustable (tunable) stability parameters. Third, the vector basis functions defined on the patches must be subjected to an orthogonalization procedure in order to ensure that they are strongly linearly independent.

It is our aim to conceive a method that simply uses nodes scattered on the domain and scalar nodal basis functions. It does not resort to vector basis functions. The divergence-free condition is enforced weakly via a Lagrange multiplier that arises naturally when the double-curl operator in the vector wave equation is replaced by the vector Laplacian. We thus arrive at a system similar to the steady-state incompressible Navier-Stokes equations of hydrodynamics [46], for which there are reliable solution methods based on nodal finite elements [47,48]. The Lagrange multiplier p together with the scattered electric field $\boldsymbol{E}^s$ constitute the unknowns of the problem. However, in this mixed formulation the electric field and the Lagrange multiplier must reside in different function spaces. It is well-known that for a mixed formulation these spaces must be compatible via the *inf-sup* condition [48,49] (a fact used in the meshfree solution of a problem in mechanics in [50]). Also, since the conducting objects that scatter the incident wave can be of any shape, we show how to embed information about the shape of the scatterer into the meshfree spaces.

Considering the imposition of the essential boundary conditions, we impose these directly as in the standard finite element method, because our nodal basis functions satisfy the Kronecker delta property at the domain boundaries.

In the following sections we propose our method and then proceed to illustrate its application in several examples. Appendix A gives some discussion of the inf-sup condition which must be satisfied in order for the discretization to be reliable.

2. The differential equations of wave scattering

Let the conducting object be represented by a closed subset $\Sigma \subset \mathbb{R}^d$, as in Fig. 1. In this work, the canonical orthonormal basis for $\mathbb{R}^d$ is represented as $\{\widehat{\boldsymbol{x}}_1, \ldots, \widehat{\boldsymbol{x}}_d\}$. The time-harmonic scattering of an electromagnetic wave by a perfect electric conductor (PEC) in free space is described in the differential formulation by the system of equations [43]:

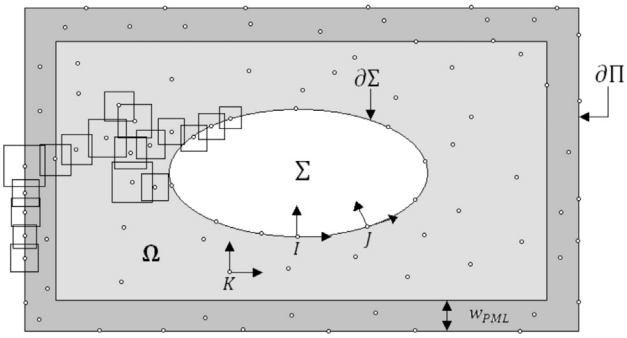

Fig. 1. The geometry of the scattering problem, illustrating the nodal distribution over the domain and along its boundary. (a) The computational domain Ω comprises the region between the outer contour $\partial\Pi$ and the surface $\partial\Sigma$ of the PEC object, which is represented by the white region (hole). (b) The PML corresponds to the layer adjacent to $\partial\Pi$. (c) The square patches, or 'overlapping elements' overlap each other (the collection of all overlapping elements associated with the nodes in the figure is not shown). (d) The patches do not conform to the geometry of the boundaries, as evidenced by the three patches at the PEC surface $\partial\Sigma$. (e) For the nodes I and J, located on $\partial\Sigma$, $\{\boldsymbol{\sigma}_1^I, \boldsymbol{\sigma}_2^I\}$ and $\{\boldsymbol{\sigma}_1^J, \boldsymbol{\sigma}_2^J\}$ are the normal and tangential unit vectors at their locations, whereas for the interior node K, $\{\boldsymbol{\sigma}_1^K, \boldsymbol{\sigma}_2^K\}$ are the unit vectors $\widehat{\boldsymbol{x}}_1$ and $\widehat{\boldsymbol{x}}_2$ along the coordinate axes X_1 and X_2, respectively. These ideas can naturally be extended to three-dimensional analysis.

$$\nabla \times \nabla \times \boldsymbol{E}^s - k_0^2 \boldsymbol{E}^s = 0, \quad in\ \Omega, \tag{1a}$$

$$\nabla \cdot \boldsymbol{E}^s = 0, \quad in\ \Omega, \tag{1b}$$

$$\widehat{\boldsymbol{n}} \times \boldsymbol{E}^s = -\widehat{\boldsymbol{n}} \times \boldsymbol{E}^{inc.}, \quad on\ \partial\Omega, \tag{1c}$$

$$\lim_{r\to\infty} \widehat{\boldsymbol{r}} \times \nabla \times \boldsymbol{E}^s = jk_0 \boldsymbol{E}^s. \tag{1d}$$

The function $\boldsymbol{E}^s : \Omega \to \mathbb{C}^d$ is a *phasor*; once it has been calculated, the real scattered electric field is given by $\boldsymbol{\mathcal{E}}^s = \mathrm{Re}\{\boldsymbol{E}^s e^{j\omega t}\}$, where $\omega = 2\pi f$ (f is the wave frequency), Re denotes the real part of a complex number, $j = \sqrt{-1}$, and t represents time. The scattering problem is stated in the unbounded domain (see Fig. 1):

$$\Omega = \mathbb{R}^d - \Sigma, \tag{1e}$$

with the boundary:

$$\partial\Omega = \partial\Sigma. \tag{1f}$$

In (1a) and (1d), $k_0 = \omega\sqrt{\mu_0 \varepsilon_0}$ is the *propagation constant* in free space; μ_0 and ε_0 are the free-space magnetic permeability and electric permittivity, respectively. Since there are no losses, k_0 is a real number. On the surface of the PEC object, the boundary conditions are given by $\widehat{\boldsymbol{n}} \times \boldsymbol{E} = 0$, where $\widehat{\boldsymbol{n}}$ is an outward-pointing unit normal vector at the surface $\partial\Omega$ of the domain (and which points towards the interior of Σ). The total electric field is $\boldsymbol{E} = \boldsymbol{E}^s + \boldsymbol{E}^{inc.}$, given by the sum of the scattered and incident fields, where the incident field is prescribed [51]. The expression in (1d) is the *radiation boundary condition*, where $\widehat{\boldsymbol{r}}$ is the unit vector in the direction of the radius vector $\boldsymbol{r}$ (from the origin $\mathcal{O}$ to any point of $\mathbb{R}^3$), and r is the Euclidean norm of $\boldsymbol{r}$, i.e., $\boldsymbol{r} = \|\boldsymbol{r}\|\widehat{\boldsymbol{r}} = r\widehat{\boldsymbol{r}}$. This condition ensures that the scattered field $\boldsymbol{E}^s$ propagates away from the PEC object [43].

The electric field in (1a) is constrained by the condition (1b), that is, Gauss' law for the free-space with no sources. To develop our formulation, we use the vector identity $\nabla \times \nabla \times \boldsymbol{E}^s = -\nabla^2 \boldsymbol{E}^s + \nabla(\nabla \cdot \boldsymbol{E}^s)$, so that (1a) becomes:

$$\nabla^2 \boldsymbol{E}^s + k_0^2 \boldsymbol{E}^s - \nabla(\nabla \cdot \boldsymbol{E}^s) = 0, \quad in\ \Omega. \tag{2}$$

Since the field $\boldsymbol{E}^s$ is described by d Cartesian components, the system formed by (2) and (1b) represents $d+1$ scalar equations in d unknowns. To introduce an additional unknown we let $p = \nabla \cdot \boldsymbol{E}^s$, so that the system of equations becomes:

$$\nabla^2 \boldsymbol{E}^s + k_0^2 \boldsymbol{E}^s - \nabla p = 0, \quad in\ \Omega. \tag{3a}$$

$$\nabla \cdot \boldsymbol{E}^s = 0, \quad in\ \Omega, \tag{3b}$$

together with the boundary conditions (1c) and (1d). These equations lead to a symmetric variational formulation and one that is similar to the variational formulation used in the solution of fluid flows [47,48]. In the solution of fluid mechanics problems, p is the physical pressure whereas here it is simply a Lagrange multiplier.

The boundary condition (1d) assumes an unbounded domain, as it takes into account distances r tending to infinity. However, since it is unfeasible to discretize an unbounded domain, we define Π to be a bounded subset of $\mathbb{R}^d$:

$$\Pi = [A_1, B_1] \times [A_2, B_2], \quad d = 2, \tag{4a}$$

$$\Pi = [A_1, B_1] \times [A_2, B_2] \times [A_3, B_3], \quad d = 3, \tag{4b}$$

with $\Sigma \subset \Pi$, as in Fig. 1. Hence Π is a parallelepiped with length $B_1 - A_1$, width $B_2 - A_2$, and height $B_3 - A_3$ sufficiently large to contain our metallic object Σ. In 2D, Π reduces to a rectangular box which contains the metallic scatterer. The scattering equations must no longer be solved in (1e), but in the new domain:

$$\Omega = \text{int}(\Pi) - \Sigma, \tag{5a}$$

where $\text{int}(\Pi)$ denotes the interior of Π. The boundary of the domain in (5a) is:

$$\partial\Omega = \partial\Pi \cup \partial\Sigma, \tag{5b}$$

i.e., $\partial\Omega$ has two components: the surface $\partial\Pi$ of the parallelepiped Π (as in Fig. 1) and the surface $\partial\Sigma$ of the PEC object (the unit vector normal to $\partial\Omega$ points toward the interior of Σ). The distance between the surfaces is given by:

$$d(\partial\Pi, \partial\Sigma) = \inf\{\|\boldsymbol{x} - \boldsymbol{y}\| : \boldsymbol{x} \in \partial\Pi, \quad \boldsymbol{y} \in \partial\Sigma\} \tag{5c}$$

In practice, depending on the problem to be solved, $d(\partial\Pi, \partial\Sigma)$ ranges from a fraction of λ_0 to a few multiples of λ_0, where $\lambda_0 = 2\pi/k_0$ is the *wavelength* associated with a plane wave whose propagation constant is given by k_0.

Since the scattered waves need to be absorbed, we introduce a *perfectly matched layer* (PML). The PML is a layer of fictitious material placed adjacent to $\partial\Pi$ in order to absorb the waves scattered by the PEC object, without reflecting them back [43]. To accommodate the PML, which has a width w_{PML} and which does not touch the PEC object, it is necessary that (see Fig. 1):

$$w_{PML} < d(\partial\Pi, \partial\Sigma). \tag{6}$$

The PML properties are given by the second-order tensor $\overline{\overline{\Lambda}}$, expressed in Cartesian coordinates as

$$\overline{\overline{\Lambda}} = \Lambda_1 \widehat{\boldsymbol{x}}_1 \widehat{\boldsymbol{x}}_1 + \cdots + \Lambda_d \widehat{\boldsymbol{x}}_d \widehat{\boldsymbol{x}}_d = \sum_{i=1}^{d} \Lambda_i \widehat{\boldsymbol{x}}_i \widehat{\boldsymbol{x}}_i. \tag{7}$$

The PML enters the problem through a modification of the wave Eq. (3a), which is now expressed as:

$$\nabla \cdot \overline{\overline{\Lambda}} \cdot \nabla \boldsymbol{E}^s + k_0^2 \boldsymbol{E}^s - \nabla p = \boldsymbol{0}, \quad in\ \Omega, \tag{8}$$

with

$$\Lambda_i(\boldsymbol{x}) = \beta_i(\boldsymbol{x}) + j\delta_i(\boldsymbol{x}), \quad \boldsymbol{x} \in \Omega, \quad i = 1, \ldots, d, \tag{9}$$

where the β_i's and the δ_i's are real-valued functions of the position within the domain.

We use the PML for solutions of scalar wave problems, see for example [52]. Given a point $\boldsymbol{x} = (x_1, \ldots, x_d)$ in the domain Ω, we define a set of distances:

$$d_i(\boldsymbol{x}) = \min\{x_i - A_i, B_i - x_i\}, \quad i = 1, \ldots, d. \tag{10}$$

Using for each $i = 1, \ldots, d$,

$$\gamma_i = \begin{cases} 1 - j\frac{1}{k_0 d_i}, & d_i \leqslant w_{PML} \\ 1, & d_i > w_{PML}, \end{cases} \tag{11}$$

the PML coefficients are calculated as:

$$\Lambda_i = \frac{1}{\gamma_i^2}, \quad i = 1, \ldots, d. \tag{12a}$$

From (11) and (12a), it can be seen that $\Lambda_i = 1$ for $d_i > w_{PML}$. On the other hand, when $d_i \leqslant w_{PML}$, we see that, for $i = 1, \ldots, d$,

$$\Lambda_i = \frac{((k_0 d_i)^2 - 1)(k_0 d_i)^2 + j2(k_0 d_i)^3}{((k_0 d_i)^2 - 1)^2 + 4(k_0 d_i)^2}. \tag{12b}$$

Examination of (12b) reveals that both the real and imaginary parts of Λ_i remain bounded when $0 \leqslant d_i \leqslant w_{PML}$. However, (12b) also shows that β_i (i.e., the real part of Λ_i) assumes negative values when $d_i < 1/k_0$. To overcome this issue, we propose a modification. Since $1/k_0$ is very small, particularly for high frequencies, the scattered waves will have already been well attenuated close to the outer boundary $\partial\Pi$. Hence, instead of (11), we use, for each $i = 1, \ldots, d$,

$$\gamma_i = \begin{cases} 1 - j\frac{1}{k_0 d_{th}}, & 0 \leqslant d_i < d_{th} \\ 1 - j\frac{1}{k_0 d_i}, & d_{th} \leqslant d_i < w_{PML} \\ 1, & d_i \geqslant w_{PML}, \end{cases} \tag{13}$$

where $d_{th} = 1.25(1/k_0)$. Of course, the *PML* width must be chosen in such a way that d_{th} is significantly smaller than w_{PML}.

We also assume that the tangential components of the scattered field $\boldsymbol{E}^s$ along $\partial\Pi$ are zero. The governing equations are now:

$$\nabla \cdot \overline{\overline{\Lambda}} \cdot \nabla \boldsymbol{E}^s + k_0^2 \boldsymbol{E}^s - \nabla p = 0, \quad in\ \Omega. \tag{14a}$$

$$\nabla \cdot \boldsymbol{E}^s = 0, \quad in\ \Omega, \tag{14b}$$

$$\widehat{\boldsymbol{n}} \times \boldsymbol{E}^s = -\widehat{\boldsymbol{n}} \times \boldsymbol{E}^{inc.}, \quad on\ \partial\Sigma, \tag{14c}$$

$$\widehat{\boldsymbol{n}} \times \boldsymbol{E}^s = 0, \quad on\ \partial\Pi, \tag{14d}$$

with $\overline{\overline{\Lambda}}$ defined as in (7), (12a), and (13). According to (14a)(14d), the scattering problem is driven by the nonhomogeneous boundary conditions along the surface $\partial\Sigma$ of the PEC object.

3. The meshfree discretization

In this section we describe the meshfree discretization we are using.

3.1. Definition of the overlapping elements

In the meshfree approach developed in this work, the shapes of the actual scatterer Σ and of its computational representation coincide, even if $\partial\Sigma$ is curved. The process of the meshfree discretization is given by these steps (see Figs. 1 and 2).

Step 1. Spread nodes throughout the interior of the domain Ω and also along the boundaries $\partial\Sigma$ and $\partial\Pi$, as shown in Fig. 1. The nodes are spread "freely" over Ω, forming a *nodal cloud* (the condition that this cloud must satisfy is stated in Step 9 below). Usually, the nodal distribution is made denser in specific regions of Ω or close to sharp boundaries.

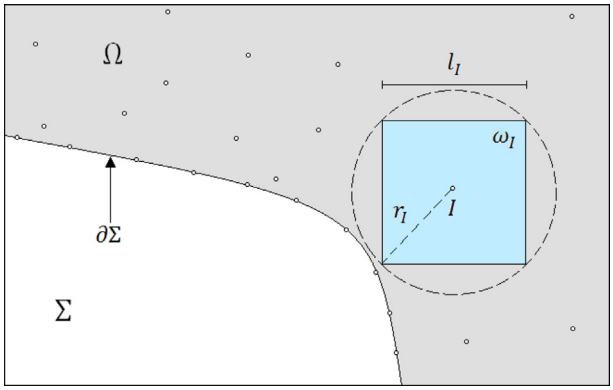

Fig. 2. The element/patch with volume ω_I associated with the interior node I. The white region represents the conducting object, whose surface is $\partial\Sigma$. This region is outside the computational domain Ω, a portion of which is represented here in grey, together with some nodes. Considering the interior node I close to the boundary $\partial\Sigma$, find its distance to $\partial\Sigma$ from (17c). Multiply this distance by 0.99, in order to get the value r_I, as in (17f). In this way, the sphere/circle centered at the node I and whose radius is given by r_I does not touch the surface $\partial\Sigma$. The patch ω_I is defined as the cube/square inscribed in this sphere/circle, here shown in light blue. The side of the cube/square is l_I.

Step 2. The number of nodes is denoted by N.

Step 3. The nodes must be numbered. They are ordered according to the natural numbers (node 1, node 2, ..., node N). The natural number associated with a given node is the *index* of the node.

Step 4. Each node is characterized by its Cartesian coordinates and by its index. So the location of node I is described as $\boldsymbol{x}^I = (x_1^I, \ldots, x_d^I)$.

Step 5. Calculate the discretization length h. First, for each node $I \in \{1, \ldots, N\}$, calculate the distance to its closest neighbor:

$$D^I = \min\{\|\boldsymbol{x}^I - \boldsymbol{x}^J\| : 1 \leqslant J \leqslant N \text{ and } J \neq I\}. \tag{15}$$

Next define h as the largest D^I:

$$h \;:=\; \max\{D^I : 1 \leqslant I \leqslant N\}. \tag{16}$$

Step 6. Consider the nodes which lie in the interior of the domain Ω, i.e., nodes whose indices are in the set:

$$Ind_\Omega \;:=\; \{I : \boldsymbol{x}^I \in \Omega\}. \tag{17a}$$

For each node I in Ind_Ω, we associate three distances. The first is the distance from node I to the *closest interior node*. This distance is calculated as

$$D_1^I = \min\{\|\boldsymbol{x}^I - \boldsymbol{x}^J\| : J \in Ind_\Omega \text{ and } J \neq I\}. \tag{17b}$$

The second is the distance between node I and the surface $\partial\Sigma$:

$$D_2^I = d(\boldsymbol{x}^I, \partial\Sigma) = \inf\{\|\boldsymbol{x}^I - \boldsymbol{y}\| : \boldsymbol{y} \in \partial\Sigma\}. \tag{17c}$$

The third is the distance between node I and the outer surface $\partial\Pi$:

$$D_3^I = d(\boldsymbol{x}^I, \partial\Pi) = \inf\{\|\boldsymbol{x}^I - \boldsymbol{y}\| : \boldsymbol{y} \in \partial\Pi\}. \tag{17d}$$

Consider now

$$s_I = \min\{\alpha D_1^I, D_2^I, D_3^I\}, \tag{17e}$$

where $\alpha > 1$, and define

$$r_I \;:=\; 0.99\; s_I. \tag{17f}$$

If one decides to employ spherical elements, then r_I can be taken as the radius of the sphere associated with node I. But since we are employing cubes instead of spheres, we use the cube of region ω_I inscribed in the sphere of radius r_I:

$$\omega_I = \prod_{i=1}^{d}\left(x_i^I - \frac{l_I}{2}, x_i^I + \frac{l_I}{2}\right), \tag{17g}$$

i.e., ω_I is the Cartesian product of open intervals centered at the node's location and whose length is l_I. The larger the α in (17e), the larger the elements will be. In this work, we choose $\alpha = \sqrt{2}$ in 2D and $\alpha = \sqrt{3}$ in 3D. The brick element defined in this way will always have its edges parallel to the coordinate axes (in this work we do not employ 'rotated' elements). Moreover, due to the fact that r_I is slightly less than s_I, *the element will not touch the boundaries* $\partial\Sigma$ *and* $\partial\Pi$ as illustrated in Fig. 2.

Step 7. Consider the nodes which lie along the surface $\partial\Sigma$ of the metallic object, i.e., nodes whose indices are in the set:

$$Ind_{\partial\Sigma} \;:=\; \{I : \boldsymbol{x}^I \in \partial\Sigma\}. \tag{18a}$$

For each node I in $Ind_{\partial\Sigma}$, we associate a single distance: the distance from node I to the *closest node also on* $\partial\Sigma$ calculated as:

$$D_1^I = \min\{\|\boldsymbol{x}^I - \boldsymbol{x}^J\| : J \in Ind_{\partial\Sigma} \text{ and } J \neq I\}, \tag{18b}$$

and define $r_I = 0.99 D_1^I$. We use here the cube inscribed in the sphere of radius r_I occupying a region represented as in (17g). *This brick element I does not include any other node from* $\partial\Sigma$.

Step 8. Consider the nodes which lie along the surface of the outer boundary $\partial\Pi$, i.e., nodes whose indices are in the set:

$$Ind_{\partial\Pi} \;:=\; \{I : \boldsymbol{x}^I \in \partial\Pi\}. \tag{19}$$

For each node I in $Ind_{\partial\Pi}$, we proceed as in Step 7.

Step 9. The collection of all N brick elements of volumes ω_I, $I = 1, \ldots, N$ must form a covering of the computational domain including the boundaries:

$$(\Omega \cup \partial\Sigma \cup \partial\Pi) = \overline{\Omega} \subset \bigcup_{I=1}^{N} \omega_I. \tag{20}$$

Here the brick elements will overlap but there shall be no 'holes' which are uncovered. One of the ways to ensure that (20) is satisfied is to spread the nodes in a reasonably balanced manner over $\overline{\Omega}$, i.e., to not allow wide portions of $\overline{\Omega}$ depopulated of nodes. For example, one could begin with a uniform distribution, and then add more nodes on and close to the boundaries (thus making the nodal cloud non-uniform in these regions).

3.2. The partition of unity

In reasonable nodal distributions, the discretization length h in (16) is much smaller than the distance between the surfaces $\partial\Sigma$ and $\partial\Pi$ defined in (5c). Therefore, any element associated with a node on the PEC surface $\partial\Sigma$ does not intersect with any element associated with a node on the outer boundary $\partial\Pi$. This fact together with the construction process given in Section 3.1 allows us to conclude that *for any node I on* $\partial\Sigma$, *the only patch to which it belongs is* ω_I. The same property holds for the nodes located along the outer boundary $\partial\Pi$.

The basis functions used in this work are based on the partition of unity paradigm [10]. The construction of the partition of unity function φ_I associated with the element I is achieved as follows:

Step 1. For $J \in \{1, \ldots, N\}$ and ω_J with edge length l_J according to (17g), define a set of d normalized distances:

$$s_1 = \frac{|x_1 - x_1^J|}{l_J/2}, \ldots, s_d = \frac{|x_d - x_d^J|}{l_J/2}, \tag{21a}$$

where $\boldsymbol{x} = (x_1, \ldots, x_d)$ is a generic point in $\overline{\Omega}$ and $\boldsymbol{x}^J = (x_1^J, \ldots, x_d^J)$ is the location of node J.

Step 2. For each value of $i = 1, \ldots, d$, evaluate the spline weight functions [10,13]:

$$w_i = \begin{cases} 1 - 6s_i^2 + 8s_i^3 - 3s_i^4, & 0 \leqslant s_i < 1, \\ 0, & s_i \geqslant 1, \end{cases} \tag{21b}$$

and define ψ_J at $\boldsymbol{x}$ as the tensor product of these w_i, i.e.,

$$\psi_J(\boldsymbol{x}) \;:=\; w_1 \ldots w_d. \tag{21c}$$

Step 3. For each $\boldsymbol{x}$ in $\overline{\Omega}$, define the sum:

$$\Psi(\boldsymbol{x}) \;:=\; \sum_{J=1}^{N} \psi_J(\boldsymbol{x}). \tag{21d}$$

Step 4. For each $I \in \{1, \ldots, N\}$ and for $\boldsymbol{x}$ in $\overline{\Omega}$, define the partition of unity function φ_I as:

$$\varphi_I(\boldsymbol{x}) \;:=\; \frac{\psi_I(\boldsymbol{x})}{\Psi(\boldsymbol{x})}. \tag{22}$$

Consider a node I on the metallic surface $\partial\Sigma$. Its location $\boldsymbol{x}^I$ is at the center of the element with volume ω_I. Since the only patch to which $\boldsymbol{x}^I$ belongs is ω_I, it follows that $\psi_J(\boldsymbol{x}^I) = 0$, for any $J \neq I$. Consequently, $\varphi_J(\boldsymbol{x}^I) = 0$, for any $J \neq I$. Moreover, since $\psi_I(\boldsymbol{x}^I) = 1$ and the function Ψ in (21d) at $\boldsymbol{x}^I$ is also equal to 1, it follows that $\varphi_I(\boldsymbol{x}^I) = 1$. The Kronecker delta property of the partition of unity functions associated with nodes on $\partial\Sigma$ thus emerges:

$$\forall I \in Ind_{\partial\Sigma} \quad \forall J \in \{1, \ldots, N\} \quad \varphi_J(\boldsymbol{x}^I) = \delta_{IJ}. \tag{23}$$

The same conclusion holds for a node I located on the boundary $\partial\Pi$.

3.3. The local spaces for each element

We associate with each element a set of M linearly independent real-valued local functions defined on ω_I:

$$p_m^I : \; \omega_I \to \mathbb{R}, \quad m = 1, \ldots, M. \tag{24}$$

The number M is the same for all patches. In this work, we shall consider only two choices for the sets of local functions.

In the first choice we make $M = 1$ and $p_1^I(\boldsymbol{x}) = 1$ in (24), so that a generic scalar function is approximated as

$$v(\boldsymbol{x}) = \sum_{I=1}^{N} \sum_{m=1}^{M} \varphi_I(\boldsymbol{x}) p_m^I(\boldsymbol{x}) \tilde{v}_{Im} = \sum_{I=1}^{N} \varphi_I(\boldsymbol{x}) \tilde{v}_{Im}, \tag{25}$$

where the coefficients $\tilde{v}_{Im}$ (which may be complex) are the degrees of freedom associated with the expansion above.

In the second choice we make $M = d + 1$ and

$$p_m^I(\boldsymbol{x}) = 1, \quad m = 1, \tag{26a}$$

$$p_m^I(\boldsymbol{x}) = \frac{x_{m-1} - x_{m-1}^I}{l_I/2}, \quad m = 2, \ldots, d+1, \tag{26b}$$

where $\boldsymbol{x} = (x_1, \ldots, x_d)$ is the point within ω_I at which the local functions are calculated and $\boldsymbol{x}^I = (x_1^I, \ldots, x_d^I)$ is the location of node I at the center of the element. The linear terms in (26b) are zero when evaluated at the location $\boldsymbol{x}^I$, i.e.,

$$p_m^I(\boldsymbol{x}^I) = 0, \quad m = 2, \ldots, d+1. \tag{26c}$$

The local terms in (26a) and (26b) will be used in the representation of a generic vector function, as described in the next section.

3.4. Spaces for approximating vector functions

The boundary conditions to be satisfied by the scattered electric field $\boldsymbol{E}^s$ in (14c) and (14d) are difficult to incorporate, because they prescribe values for the tangential components only, whereas the normal components are left unspecified. If we simply declare that each Cartesian component $E_1^s, \ldots, E_d^s$ should be discretized separately, there may be difficulties when imposing the conditions for the tangential component when the boundary is a curved surface, because the normal and tangential unit vectors at the surface do not always coincide with the canonical basis vectors $\widehat{\boldsymbol{x}}_1, \ldots, \widehat{\boldsymbol{x}}_d$. In order to overcome these difficulties, we devised the approximation scheme below.

To each node I located at $\boldsymbol{x}^I$, in addition to the cubic patch ω_I and the local terms from (26a) and (26b), we ascribe a set of d linearly independent unit vectors $\{\boldsymbol{\sigma}_1^I, \ldots, \boldsymbol{\sigma}_d^I\}$, which form a local basis for $\mathbb{R}^d$. These vectors are determined as follows.

Case 1. $d = 2$. If $I \in Ind_\Omega$, i.e., if I is an interior node, then

$$\boldsymbol{\sigma}_1^I = \widehat{\boldsymbol{x}}_1, \tag{27a}$$

$$\boldsymbol{\sigma}_2^I = \widehat{\boldsymbol{x}}_2,$$

i.e., $\boldsymbol{\sigma}_1^I$ and $\boldsymbol{\sigma}_2^I$ are just the canonical unit vectors along the x_1 and x_2 axes, respectively. If I belongs to either $Ind_{\partial\Sigma}$ or $Ind_{\partial\Pi}$, i.e., if I is located on the boundaries, then we use the outward-pointing unit normal vector $\widehat{\boldsymbol{n}}$ on the surfaces $\partial\Sigma$ and $\partial\Pi$, and so we employ

$$\boldsymbol{\sigma}_1^I = \widehat{\boldsymbol{n}}. \tag{27b}$$

i.e., $\boldsymbol{\sigma}_1^I$ is the normal vector $\widehat{\boldsymbol{n}}$ calculated at the node location $\boldsymbol{x}^I$. The second vector $\boldsymbol{\sigma}_2^I$ is made equal to a tangent vector at $\boldsymbol{x}^I$. This tangent vector can be taken as

$$\boldsymbol{\sigma}_2^I = \widehat{\boldsymbol{x}}_3 \times \boldsymbol{\sigma}_1^I, \tag{27c}$$

where $\widehat{\boldsymbol{x}}_3 = (0, 0, 1)$ is the unit vector along axis x_3 (perpendicular to the plane in which a 2D problem is defined). Fig. 1 gives an illustration of nodes I, J, and K, and their associated basis vectors $\{\boldsymbol{\sigma}_1^I, \boldsymbol{\sigma}_2^I\}$, $\{\boldsymbol{\sigma}_1^J, \boldsymbol{\sigma}_2^J\}$, and $\{\boldsymbol{\sigma}_1^K, \boldsymbol{\sigma}_2^K\}$, respectively.

Case 2. $d = 3$. If $I \in Ind_\Omega$, then

$$\boldsymbol{\sigma}_1^I = \widehat{\boldsymbol{x}}_1, \tag{27d}$$

$$\boldsymbol{\sigma}_2^I = \widehat{\boldsymbol{x}}_2,$$

$$\boldsymbol{\sigma}_3^I = \widehat{\boldsymbol{x}}_3.$$

If I belongs to either $Ind_{\partial\Sigma}$ or $Ind_{\partial\Pi}$, then

$$\boldsymbol{\sigma}_1^I = \widehat{\boldsymbol{n}}. \tag{27e}$$

In order to determine the other two vectors, we proceed as follows. Let $\boldsymbol{b}$ be any vector not parallel to $\widehat{\boldsymbol{n}}$, i.e., $\boldsymbol{b} - (\boldsymbol{b} \cdot \widehat{\boldsymbol{n}})\widehat{\boldsymbol{n}} \neq 0$. Then we use $\boldsymbol{w} = \boldsymbol{b} - (\boldsymbol{b} \cdot \widehat{\boldsymbol{n}})\widehat{\boldsymbol{n}}$ and

$$\boldsymbol{\sigma}_2^I = \frac{\boldsymbol{w}}{\|\boldsymbol{w}\|}. \tag{27f}$$

Clearly, $\boldsymbol{\sigma}_2^I$ is perpendicular to $\widehat{\boldsymbol{n}}$ and therefore is tangential to the surface in question. The other vector $\boldsymbol{\sigma}_3^I$ is determined simply by

$$\boldsymbol{\sigma}_3^I = \boldsymbol{\sigma}_1^I \times \boldsymbol{\sigma}_2^I. \tag{27g}$$

From the cross product above, it is clear that $\boldsymbol{\sigma}_3^I$ is perpendicular to the normal $\boldsymbol{\sigma}_1^I = \widehat{\boldsymbol{n}}$, and thus it is also tangential to the surface in question. It is also clear that $\boldsymbol{\sigma}_3^I$ is perpendicular to $\boldsymbol{\sigma}_2^I$. In this way, $\boldsymbol{\sigma}_1^I$ is a unit vector normal to the surface, whereas $\boldsymbol{\sigma}_2^I$ and $\boldsymbol{\sigma}_3^I$

are both mutually perpendicular and tangential to the surface. The set $\{\boldsymbol{\sigma}_1^I, \boldsymbol{\sigma}_2^I, \boldsymbol{\sigma}_3^I\}$ thus forms a local basis for $\mathbb{R}^3$ at the point $\boldsymbol{x}^I$.

After the local basis vectors $\{\boldsymbol{\sigma}_1^I, \ldots, \boldsymbol{\sigma}_d^I\}$ have been determined for all nodes any generic vector field $\boldsymbol{v}$ is discretized as:

$$\boldsymbol{v}(\boldsymbol{x}) = \sum_{I=1}^{N}\sum_{m=1}^{d+1}\varphi_I(\boldsymbol{x})p_m^I(\boldsymbol{x})(\boldsymbol{\sigma}_1^I\tilde{v}_{Im}^1 + \cdots + \boldsymbol{\sigma}_d^I\tilde{v}_{Im}^d) \tag{28a}$$

The expansion (28a) is to be interpreted as follows: Inside each element, there are d mutually orthogonal unit vectors $\boldsymbol{\sigma}_1^I, \ldots, \boldsymbol{\sigma}_d^I$, and the coefficients $\tilde{v}_{Im}^1$ (which may be complex) govern the amplitude of $\boldsymbol{v}$ along $\boldsymbol{\sigma}_1^I$, whereas the $\tilde{v}_{Im}^2$ govern the amplitude of $\boldsymbol{v}$ along $\boldsymbol{\sigma}_2^I$, and so on. In a more compact form, (28a) becomes:

$$\boldsymbol{v}(\boldsymbol{x}) = \sum_{I=1}^{N}\sum_{m=1}^{d+1}\sum_{k=1}^{d}h_{Im}(\boldsymbol{x})\boldsymbol{\sigma}_k^I\tilde{v}_{Im}^k, \tag{28b}$$

where we write, as in [10],

$$h_{Im}(\boldsymbol{x}) = \varphi_I(\boldsymbol{x})p_m^I(\boldsymbol{x}), \tag{28c}$$

4. Meshfree discretization of the scattering system

We have the basic spaces $L^2(\Omega;\mathbb{K})$ and $H^1(\Omega;\mathbb{K})$ [53–55]:

$$u \in L^2(\Omega;\mathbb{K}) \iff \begin{cases} u : \Omega \to K, \\ \int_\Omega |u|^2 d\Omega < \infty, \end{cases} \tag{29a}$$

$$u \in H^1(\Omega;\mathbb{K}) \iff \begin{cases} u \in L^2(\Omega;\mathbb{K}), \\ \partial_i u \in L^2(\Omega;\mathbb{K}), \quad i = 1, \ldots, d, \end{cases} \tag{29b}$$

where $\iff$ means 'if and only if', $\mathbb{K} = \mathbb{R}$ or $\mathbb{K} = \mathbb{C}$, and u is a scalar field. Consider the following spaces of complex-valued functions:

$$\mathbb{E} = \Big\{\boldsymbol{v} \in H^1(\Omega;\mathbb{C})^d : \widehat{\boldsymbol{n}} \times \boldsymbol{v}|_{\partial\Sigma} = -\widehat{\boldsymbol{n}} \times \boldsymbol{E}^{inc.}, \quad \widehat{\boldsymbol{n}} \times \boldsymbol{v}|_{\partial\Pi} = 0\Big\}, \tag{29c}$$

$$\mathbb{V} = \Big\{\boldsymbol{v} \in H^1(\Omega;\mathbb{C})^d : \widehat{\boldsymbol{n}} \times \boldsymbol{v}|_{\partial\Sigma} = 0, \quad \widehat{\boldsymbol{n}} \times \boldsymbol{v}|_{\partial\Pi} = 0\Big\}, \tag{29d}$$

$$\mathbb{P} = L^2(\Omega;\mathbb{C}). \tag{29e}$$

In (29a), $L^2(\Omega;\mathbb{K})$ is the linear space whose elements are real or complex-valued functions which are square integrable (in the sense of Lebesgue) on Ω. In (29b), where $\partial_i u = \partial u/\partial x_i$, $H^1(\Omega;\mathbb{K})$ denotes the linear space of real or complex-valued functions whose weak first derivatives are square integrable on Ω [53–55]. In (29c) and (29d), $H^1(\Omega;\mathbb{C})^d$ is the Cartesian product of $H^1(\Omega;\mathbb{C})$ with itself d times. The elements of the space $\mathbb{E}$ in (29c) will be useful in representing weak solutions for the scattered electric field $\boldsymbol{E}^s$, whereas the linear space $\mathbb{V}$ in (29d) will be employed as a space of test functions. Finally, the elements of the space $\mathbb{P}$ in (29e) will represent weak solutions for the Lagrange multiplier p.

Because the local terms p_m^I in (26a) and (26b) are (first degree) polynomials, it follows from [10] that each term $\varphi_I p_m^I$ in (28a) belongs to $H^1(\Omega;\mathbb{R})$, or according to (28c),

$$h_{Im} \in H^1(\Omega;\mathbb{R}), \quad I = 1, \ldots, N, \quad m = 1, \ldots, d+1. \tag{30}$$

We thus define the discretized version of $\mathbb{E}$ in (29c) through the rule:

$$\boldsymbol{v}_h \in \mathbb{E}_h \iff \begin{cases} \boldsymbol{v}_h = \sum_{Imk} h_{Im}\boldsymbol{\sigma}_k^I\tilde{v}_{Im}^k, \\ \tilde{v}_{Im}^k \in \mathbb{C}, \\ \widehat{\boldsymbol{n}} \times \boldsymbol{v}_h|_{\partial\Sigma} = -\widehat{\boldsymbol{n}} \times \boldsymbol{E}^{inc.}, \\ \widehat{\boldsymbol{n}} \times \boldsymbol{v}_h|_{\partial\Pi} = \boldsymbol{0}, \end{cases} \tag{31a}$$

i.e., a vector $\boldsymbol{v}_h$ belongs to $\mathbb{E}_h$ if and only if $\boldsymbol{v}_h$ admits an expansion as (28b) in which the degrees of freedom $\tilde{v}_{Im}^k$ are complex, and if $\boldsymbol{v}_h$ satisfies the boundary conditions (14c) and (14d) along $\partial\Sigma$ and $\partial\Pi$, respectively. Using (30), we find that $\mathbb{E}_h \subset \mathbb{E}$.

The discretized version of $\mathbb{V}$ in (29d) is defined as:

$$\boldsymbol{v}_h \in \mathbb{V}_h \iff \begin{cases} \boldsymbol{v}_h = \sum_{Imk} h_{Im}\boldsymbol{\sigma}_k^I\tilde{v}_{Im}^k, \\ \tilde{v}_{Im}^k \in \mathbb{C}, \\ \widehat{\boldsymbol{n}} \times \boldsymbol{v}_h|_{\partial\Sigma} = \boldsymbol{0}, \\ \widehat{\boldsymbol{n}} \times \boldsymbol{v}_h|_{\partial\Pi} = \boldsymbol{0}. \end{cases} \tag{31b}$$

The spaces $\mathbb{E}_h$ and $\mathbb{V}_h$ differ only in the boundary conditions along the metallic surface $\partial\Sigma$: they are nonhomogeneous in $\mathbb{E}_h$ and homogeneous in $\mathbb{V}_h$. It can also be shown that $\mathbb{V}_h \subset \mathbb{V}$. Finally, the discretized version of $\mathbb{P}$ in (29e) is given by:

$$q_h \in \mathbb{P}_h \iff \begin{cases} q_h = \sum_{I=1}^{N}\varphi_I\tilde{q}_I, \\ \tilde{q}_I \in \mathbb{C}, \end{cases} \tag{31c}$$

i.e., $q_h \in \mathbb{P}_h$ if and only if q_h admits an expansion as (25). Here only the functions φ_I are used, the coefficients $\tilde{q}_I$ are complex, and there are no boundary conditions to be satisfied by the elements of $\mathbb{P}_h$. We can show that $\mathbb{P}_h \subset \mathbb{P}$.

In order to transform the governing Eqs. (14a)–(14d) into the weak form, we apply the weighted residual procedure. First, we dot multiply (14a) by the complex conjugate of an arbitrary test function $\boldsymbol{v}$ from the space $\mathbb{V}$ in (29d) and integrate over the domain Ω. Second, we multiply (14b) by the complex conjugate of an arbitrary test function q from the space $\mathbb{P}$ in (29e) and integrate over Ω. We obtain the following problem stated for the infinite-dimensional spaces $\mathbb{E}$, $\mathbb{V}$, and $\mathbb{P}$:

Find $(\boldsymbol{E}^s, p) \in \mathbb{E} \times \mathbb{P}$ *such that*

$$\int_\Omega ((\overline{\overline{\boldsymbol{\Lambda}}} \cdot \nabla\boldsymbol{E}^s) : \nabla\boldsymbol{v}^* - k_0^2\boldsymbol{E}^s \cdot \boldsymbol{v}^*)d\Omega - \int_\Omega p\nabla \cdot \boldsymbol{v}^* d\Omega - \oint_{\partial\Omega}((\overline{\overline{\boldsymbol{\Lambda}}} \cdot \nabla\boldsymbol{E}^s) \cdot \widehat{\boldsymbol{n}} - p\widehat{\boldsymbol{n}}) \cdot \boldsymbol{v}^* d\Gamma = 0, \quad \forall\boldsymbol{v} \in \mathbb{V}. \tag{32a}$$

$$\int_\Omega q^*\nabla \cdot \boldsymbol{E}^s d\Omega = 0, \quad \forall q \in \mathbb{P}, \tag{32b}$$

where $d\Omega$ denotes a volume (area) element and $d\Gamma$ a surface (line) element in three (two) dimensions, respectively, and $\partial\Omega = \partial\Sigma \cup \partial\Pi$.

In the formulation the Lagrange multiplier p does not have a physical meaning; it was included to couple Eqs. (2) and (1b), and there are so far no boundary conditions to be satisfied by p. Therefore we simply use that on $\partial\Omega$, p is such that the boundary integral in (32a) disappears. The problem assumes the new form:

Find $(\boldsymbol{E}^s, p) \in \mathbb{E} \times \mathbb{P}$ *such that*

$$\int_\Omega ((\overline{\overline{\boldsymbol{\Lambda}}} \cdot \nabla\boldsymbol{E}^s) : \nabla\boldsymbol{v}^* - k_0^2\boldsymbol{E}^s \cdot \boldsymbol{v}^*)d\Omega - \int_\Omega p\nabla \cdot \boldsymbol{v}^* d\Omega = 0, \quad \forall\boldsymbol{v} \in \mathbb{V}. \tag{32c}$$

$$\int_\Omega q^*\nabla \cdot \boldsymbol{E}^s d\Omega = 0, \quad \forall q \in \mathbb{P}. \tag{32d}$$

Because (14a) includes just the gradient of p, one could in principle argue that, if $(\boldsymbol{E}^s, p)$ is a solution to (14a)–(14d), then $(\boldsymbol{E}^s, p+c)$, where c is a nonzero constant, is also a solution, because $\nabla c = 0$. This does not hold for the weak problem (32c) and (32d), as the reasoning below shows.

Let $(\boldsymbol{E}^s, p)$ be a solution to (32c) and (32d).

Suppose that $(\boldsymbol{E}^s, p+c)$ is also a solution to (32c) and (32d).

When we replace p by $p+c$ in (32c), we are left with the integral expression:

$$\int_\Omega c\nabla\cdot\boldsymbol{v}^* d\Omega = 0, \quad \forall \boldsymbol{v}\in\mathbb{V}. \tag{32e}$$

Since c is a constant, (32e) is equal to:

$$c\int_\Omega \nabla\cdot\boldsymbol{v}^* d\Omega = c\oint_{\partial\Omega}\boldsymbol{v}^*\cdot\hat{\boldsymbol{n}} d\Gamma = 0, \quad \forall \boldsymbol{v}\in\mathbb{V}. \tag{32f}$$

Since the elements of the test space $\mathbb{V}$ in (29d) have zero *tangential* components, but not zero *normal* components, the boundary integral in (32f) is not always equal to zero. Consequently (32f) holds for any $\boldsymbol{v}$ iff $c=0$. ■

The Lagrange multiplier p is therefore uniquely determined. This is in contrast to solving the Stokes and Navier-Stokes equations where the pressure must be specified at a point or by applied tractions [48].

Because $\mathbb{V}_h \subset \mathbb{V}$ and $\mathbb{P}_h \subset \mathbb{P}$, (32c) and (32d) still hold when the test functions in $\mathbb{V}$ and $\mathbb{P}$ are replaced by those in $\mathbb{V}_h$ and $\mathbb{P}_h$, respectively. However, since our meshfree solutions will be approximated by elements from the discretized spaces $\mathbb{E}_h$ and $\mathbb{P}_h$, we obtain:

Find $(\boldsymbol{E}^s_h, p_h)\in\mathbb{E}_h\times\mathbb{P}_h$ *such that*

$$\int_\Omega ((\overline{\overline{\Lambda}}\cdot\nabla\boldsymbol{E}^s_h):\nabla\boldsymbol{v}^*_h - k_0^2\boldsymbol{E}^s_h\cdot\boldsymbol{v}^*_h)d\Omega - \int_\Omega p_h\nabla\cdot\boldsymbol{v}^*_h d\Omega = 0, \quad \forall\boldsymbol{v}_h\in\mathbb{V}_h. \tag{33a}$$

$$\int_\Omega q^*_h\nabla\cdot\boldsymbol{E}^s_h d\Omega = 0, \quad \forall q_h\in\mathbb{P}_h. \tag{33b}$$

5. The imposition of boundary conditions

By the construction of the discretization, the behavior of the discretized fields on the boundaries depends only on the element unknowns on the boundaries (i.e., coefficients associated with nodes from the index sets $Ind_{\partial\Sigma}$ and $Ind_{\partial\Pi}$ in (18a) and (19), respectively).

Consider the discretized electric field $\boldsymbol{E}^s_h\in\mathbb{E}_h$. According to (31a), it can be expressed as:

$$\boldsymbol{E}^s_h(\boldsymbol{x}) = \sum_{I=1}^{N}\sum_{m=1}^{d+1}\sum_{k=1}^{d} h_{Im}(\boldsymbol{x})\boldsymbol{\sigma}^I_k\widetilde{E}^k_{Im}. \tag{34a}$$

We want to determine the coefficients $\widetilde{E}^k_{Im}$ for nodes on the boundaries. Let J be any node on the metallic surface $\partial\Sigma$, i.e., $J\in Ind_{\partial\Sigma}$. From the boundary condition along $\partial\Sigma$ in (31a), at the node location $\boldsymbol{x}^J$ we have:

$$\sum_{I=1}^{N}\sum_{m=1}^{d+1}\sum_{k=1}^{d} h_{Im}(\boldsymbol{x}^J)(\hat{\boldsymbol{n}}\times\boldsymbol{\sigma}^I_k)\widetilde{E}^k_{Im} = -\hat{\boldsymbol{n}}\times\boldsymbol{E}^{inc.}(\boldsymbol{x}^J) \tag{34b}$$

From (28c) and (23),

$$\sum_{m=1}^{d+1}\sum_{k=1}^{d} p^J_m(\boldsymbol{x}^J)(\hat{\boldsymbol{n}}\times\boldsymbol{\sigma}^J_k)\widetilde{E}^k_{Jm} = -\hat{\boldsymbol{n}}\times\boldsymbol{E}^{inc.}(\boldsymbol{x}^J). \tag{34c}$$

Properties (26c) and (26a) allow this to be simplified to:

$$\sum_{k=1}^{d}(\hat{\boldsymbol{n}}\times\boldsymbol{\sigma}^J_k)\widetilde{E}^k_{J1} = -\hat{\boldsymbol{n}}\times\boldsymbol{E}^{inc.}(\boldsymbol{x}^J). \tag{34d}$$

Both two and three dimensional situations will be investigated.

Case 1: $d=2$. Because $\hat{\boldsymbol{n}} = \boldsymbol{\sigma}^J_1$ from (27b), expression (34d) becomes:

$$(\boldsymbol{\sigma}^J_1\times\boldsymbol{\sigma}^J_2)\widetilde{E}^2_{J1} = -\boldsymbol{\sigma}^J_1\times\boldsymbol{E}^{inc.}(\boldsymbol{x}^J). \tag{34e}$$

With the help of (27c) and the vector product identity $\boldsymbol{a}\cdot(\boldsymbol{b}\times\boldsymbol{c}) = \boldsymbol{c}\cdot(\boldsymbol{a}\times\boldsymbol{b})$, we obtain the coefficient:

$$\widetilde{E}^2_{J1} = -\boldsymbol{E}^{inc.}(\boldsymbol{x}^J)\cdot\boldsymbol{\sigma}^J_2. \tag{34f}$$

Case 2: $d=3$. We know that $\hat{\boldsymbol{n}} = \boldsymbol{\sigma}^J_1$ from (27e) and (34d) becomes:

$$(\boldsymbol{\sigma}^J_1\times\boldsymbol{\sigma}^J_2)\widetilde{E}^2_{J1} + (\boldsymbol{\sigma}^J_1\times\boldsymbol{\sigma}^J_3)\widetilde{E}^3_{J1} = -\boldsymbol{\sigma}^J_1\times\boldsymbol{E}^{inc.}(\boldsymbol{x}^J). \tag{34g}$$

With the help of (27g), we obtain:

$$\boldsymbol{\sigma}^J_3\widetilde{E}^2_{J1} - \boldsymbol{\sigma}^J_2\widetilde{E}^3_{J1} = -\boldsymbol{\sigma}^J_1\times\boldsymbol{E}^{inc.}(\boldsymbol{x}^J). \tag{34h}$$

Now we dot multiply (34h) by $\boldsymbol{\sigma}^J_3$ and apply the aforementioned vector identity. We repeat the process for $\boldsymbol{\sigma}^J_2$, and arrive at the values of the coefficients:

$$\widetilde{E}^2_{J1} = -\boldsymbol{E}^{inc.}(\boldsymbol{x}^J)\cdot\boldsymbol{\sigma}^J_2, \tag{34i}$$

$$\widetilde{E}^3_{J1} = -\boldsymbol{E}^{inc.}(\boldsymbol{x}^J)\cdot\boldsymbol{\sigma}^J_3.$$

From (34f) and (34i), we see that for a node J on the boundary $\partial\Sigma$, the unknowns relative to the tangential directions ($\boldsymbol{\sigma}^J_2$ in 2D; $\boldsymbol{\sigma}^J_2$ and $\boldsymbol{\sigma}^J_3$ in 3D) and associated with the constant term ($m=1$) in the local space have been determined. We set the linearly varying terms to zero and thus have:

If $I\in Ind_{\partial\Sigma}$ *and* $k=2,\ldots,d$: (34j)

$$\widetilde{E}^k_{Im} = -\boldsymbol{E}^{inc.}(\boldsymbol{x}^J)\cdot\boldsymbol{\sigma}^I_k, \quad m=1,$$

$$\widetilde{E}^k_{Im} = 0, \qquad m=2,\ldots,d+1.$$

Likewise, considering the nodes on the outer surface $\partial\Pi$, given the boundary condition in (31a) we obtain:

If $I\in Ind_{\partial\Pi}$ *and* $k=2,\ldots,d$: (34k)

$$\widetilde{E}^k_{Im} = 0, \quad m=1,\ldots,d+1.$$

When we consider an arbitrary element $\boldsymbol{v}_h$ from the discretized test space $\mathbb{V}_h$, all coefficients associated with tangential directions in the nodes located on the boundaries $\partial\Sigma$ and $\partial\Pi$ are zero, because the boundary conditions in (31b) are homogeneous on both surfaces $\partial\Sigma$ and $\partial\Pi$.

The scattering system (33a) and (33b) is not symmetric since the solution is sought in $\mathbb{E}_h$, whereas the test functions are in $\mathbb{V}_h$. Symmetry is reached as in the traditional finite element analysis [41,48,56]. Namely, given any $\boldsymbol{E}^s_h\in\mathbb{E}_h$, we write:

$$\boldsymbol{E}^s_h = \boldsymbol{u}_h + \boldsymbol{e}^0_h, \tag{35a}$$

where $\boldsymbol{u}_h\in\mathbb{V}_h$. The *lifting* function $\boldsymbol{e}^0_h\in\mathbb{E}_h$ satisfies the same boundary conditions as $\boldsymbol{E}^s_h$. It is expanded as:

$$\boldsymbol{e}^0_h(\boldsymbol{x}) = \sum_{I=1}^{N}\sum_{m=1}^{d+1}\sum_{k=1}^{d} h_{Im}(\boldsymbol{x})\boldsymbol{\sigma}^I_k\tilde{e}^k_{Im}. \tag{35b}$$

Using the known incident field $\boldsymbol{E}^{inc.}$, we can choose $\boldsymbol{e}_h^0$ so that all coefficients $\tilde{e}_{lm}^k$ are zero, except those associated with the tangential directions in the boundary nodes, which are determined by the rule (34j), (34k). Substituting (35a) into (33a) and (33b), $\boldsymbol{u}_h$ becomes the new unknown, and the problem assumes the symmetric form:

Find $(\boldsymbol{u}_h, p_h) \in \mathbb{V}_h \times \mathbb{P}_h$ *such that*

$$\int_\Omega ((\overline{\overline{\boldsymbol{\Lambda}}} \cdot \nabla \boldsymbol{u}_h) : \nabla \boldsymbol{v}_h^* - k_0^2 \boldsymbol{u}_h \cdot \boldsymbol{v}_h^*) d\Omega - \int_\Omega p_h \nabla \cdot \boldsymbol{v}_h^* d\Omega = -\int_\Omega ((\overline{\overline{\boldsymbol{\Lambda}}} \cdot \nabla \boldsymbol{e}_h^0) : \nabla \boldsymbol{v}_h^* - k_0^2 \boldsymbol{e}_h^0 \cdot \boldsymbol{v}_h^*) d\Omega, \quad \forall \boldsymbol{v}_h \in \mathbb{V}_h, \tag{36a}$$

$$-\int_\Omega q_h^* \nabla \cdot \boldsymbol{u}_h d\Omega = \int_\Omega q_h^* \nabla \cdot \boldsymbol{e}_h^0 d\Omega, \quad \forall q_h \in \mathbb{P}_h. \tag{36b}$$

It should be noted that in practice we do not explicitly use a lifting function but simply establish the governing equations with all boundary conditions removed and then apply these boundary conditions in the assemblage phase [48]. This is of course equivalent in theory to the use of a lifting function.

We introduce the *sesquilinear* (or semilinear) forms $a : \mathbb{V}_h \times \mathbb{V}_h \to \mathbb{C}$, and $b : \mathbb{V}_h \times \mathbb{P}_h \to \mathbb{C}$ given by:

$$a(\boldsymbol{u}_h, \boldsymbol{v}_h) = \int_\Omega ((\overline{\overline{\boldsymbol{\Lambda}}} \cdot \nabla \boldsymbol{u}_h) : \nabla \boldsymbol{v}_h^* - k_0^2 \boldsymbol{u}_h \cdot \boldsymbol{v}_h^*) d\Omega, \tag{36c}$$

$$b(\boldsymbol{v}_h, q_h) = -\int_\Omega q_h^* \nabla \cdot \boldsymbol{v}_h d\Omega, \tag{36d}$$

where by sesquilinear we mean that

$$a(\alpha_1 \boldsymbol{u}_1 + \alpha_2 \boldsymbol{u}_2, \boldsymbol{v}) = \alpha_1 a(\boldsymbol{u}_1, \boldsymbol{v}) + \alpha_2 (\boldsymbol{u}_2, \boldsymbol{v}), \tag{36e}$$

$$a(\boldsymbol{u}, \alpha_1 \boldsymbol{v}_1 + \alpha_2 \boldsymbol{v}_2) = \alpha_1^* a(\boldsymbol{u}, \boldsymbol{v}_1) + \alpha_2^* (\boldsymbol{u}, \boldsymbol{v}_2),$$

for any $\boldsymbol{u}_1, \boldsymbol{u}_2, \boldsymbol{v} \in \mathbb{V}_h$ and $\alpha_1, \alpha_2 \in \mathbb{C}$. The form b in (36d) satisfies these same properties. Introduce also the functionals $F : \mathbb{V}_h \to \mathbb{C}$ and $G : \mathbb{P}_h \to \mathbb{C}$ given by:

$$F(\boldsymbol{v}_h) = -\int_\Omega ((\overline{\overline{\boldsymbol{\Lambda}}} \cdot \nabla \boldsymbol{e}_h^0) : \nabla \boldsymbol{v}_h^* - k_0^2 \boldsymbol{e}_h^0 \cdot \boldsymbol{v}_h^*) d\Omega, \tag{36f}$$

$$G(q_h) = \int_\Omega q_h^* \nabla \cdot \boldsymbol{e}_h^0 d\Omega. \tag{36g}$$

The problem in (36a) and (36b) can therefore be written as:

Find $(\boldsymbol{u}_h, p_h) \in \mathbb{V}_h \times \mathbb{P}_h$ *such that*

$$\begin{aligned} a(\boldsymbol{u}_h, \boldsymbol{v}_h) + b(\boldsymbol{v}_h, p_h)^* &= F(\boldsymbol{v}_h), \quad \forall \boldsymbol{v}_h \in \mathbb{V}_h, \\ b(\boldsymbol{u}_h, q_h) &= G(q_h), \quad \forall q_h \in \mathbb{P}_h. \end{aligned} \tag{37}$$

The problem in (37) is readily seen to be cast in a *mixed or hybrid formulation*, and constitutes a *saddle-point problem*. The form (37) is a model for many problems in computational mechanics, and both its theoretical and practical aspects have been amply discussed [48,49,57–59]. The well-posedness of the problem (37) specialized to the sesquilinear forms (36c) and (36d) is addressed in Appendix A.

Using the discretized vector functions $\boldsymbol{u}_h$ and $\boldsymbol{v}_h$ as

$$\boldsymbol{u}_h = \sum_{J=1}^{N} \sum_{n=1}^{d+1} \sum_{l=1}^{d} h_{Jn} \boldsymbol{\sigma}_l^J \tilde{u}_{Jn}^l, \quad \boldsymbol{v}_h = \sum_{I=1}^{N} \sum_{m=1}^{d+1} \sum_{k=1}^{d} h_{Im} \boldsymbol{\sigma}_k^I \tilde{v}_{Im}^k, \tag{38a}$$

the discretized scalar functions p_h and q_h as

$$p_h = \sum_{J=1}^{N} \varphi_J \tilde{p}_J, \quad q_h = \sum_{I=1}^{N} \varphi_I \tilde{q}_I, \tag{38b}$$

and substituting into the system of Eqs. (36a), (36b), we obtain the linear system

$$\boldsymbol{K}\boldsymbol{U} = \boldsymbol{F}. \tag{39}$$

Here $\boldsymbol{K}$ is the governing matrix of the discretized problem, $\boldsymbol{U}$ the solution vector and $\boldsymbol{F}$ the forcing vector. The matrix $\boldsymbol{K}$ is sparse, and its entries are evaluated numerically. For the numerical evaluation we subdivide the edge of element I into n_{sub} equal lengths, so that each subdivision has a length given by $\Delta l = l_I / n_{sub}$. Hence in 2D analyses, the element volume is divided into $(n_{sub})^2$ equal little squares, over which we integrate with the 1 or 2 point Gauss rules. In 3D analyses we proceed in the same way.

In the assemblage of $\boldsymbol{K}$ and $\boldsymbol{F}$ we use the fact that the homogeneous boundary conditions are satisfied by $\boldsymbol{u}_h \in \mathbb{V}_h$ and do not assemble the rows and columns corresponding to the boundary degrees of freedom [48]. Solving (39) gives the coefficients $\tilde{u}_{Jn}^l$ in the expansion of $\boldsymbol{u}_h$, and the scattered field $\boldsymbol{E}_h^s$ can be calculated at any point in the domain Ω by adding $\boldsymbol{u}_h$ and the lifting function $\boldsymbol{e}_h^0$, according to (35a).

6. Numerical solutions

In this section we present the solutions to various problems in order to illustrate the capabilities of the presented solution scheme.

6.1. A Maxwell eigenproblem

The formulation developed in the previous sections can be easily adapted to treat the Maxwell eigenvalue problem. Suppose $\Omega \subset \mathbb{R}^d$ is a bounded domain, which represents the interior of a hollow cavity bounded by a perfectly conducting surface $\partial\Omega$. The Maxwell eigenvalue problem is given by [51]:

$$\nabla \times \nabla \times \boldsymbol{E} = k_0^2 \boldsymbol{E}, \quad in\ \Omega, \tag{40a}$$

$$\nabla \cdot \boldsymbol{E} = 0, \quad in\ \Omega, \tag{40b}$$

$$\widehat{\boldsymbol{n}} \times \boldsymbol{E} = \boldsymbol{0}, \quad on\ \partial\Omega. \tag{40c}$$

There are differences between the eigenvalue problem (40a)–(40c) and the scattering problem (1a)–(1d). First, the unknown is the total electric field $\boldsymbol{E}$ instead of the scattered field $\boldsymbol{E}^s$. Second, there is no need to deal with the behavior of the field at very large distances. Third, the wavenumber k_0 is not known in advance; rather, it is one of the unknowns of the problem. For hollow cavities, k_0 is a positive real number. Fourth, the electric field $\boldsymbol{E}$ is a real-valued quantity, and not a complex-valued quantity as $\boldsymbol{E}^s$. Among the resemblances between the two problems, we point out the fact that both are subjected to a divergence-free constraint, and that the boundary conditions are prescribed for the tangential components of the vector fields only.

In this work, we are not focusing on the eigenvalue problem, but consider it as a test to provide some insight into the approximability properties of our meshfree spaces.

Following the above derivation we arrive at the discretized problem:

Find $(\boldsymbol{E}_h, p_h, k_0) \in \mathbb{V}_h \times \mathbb{P}_h \times \mathbb{R}^+$ *such that*

$$\int_\Omega \nabla \boldsymbol{E}_h : \nabla \boldsymbol{v}_h^* d\Omega - \int_\Omega p_h \nabla \cdot \boldsymbol{v}_h^* d\Omega = k_0^2 \int_\Omega \boldsymbol{E}_h \cdot \boldsymbol{v}_h^* d\Omega, \quad \forall \boldsymbol{v}_h \in \mathbb{V}_h \tag{41a}$$

$$\int_\Omega q_h^* \nabla \cdot \boldsymbol{E}_h d\Omega = 0, \quad \forall q_h \in \mathbb{P}_h. \tag{41b}$$

The spaces $\mathbb{V}_h$ and $\mathbb{P}_h$ are those of (31b) and (31c), respectively. The only difference is that we can assume the eigenfunctions $\boldsymbol{E}_h$ to be real-valued, so that the coefficients in the expansion of the solution are real numbers.

The quantities $\boldsymbol{E}_h$, $\boldsymbol{v}_h$, p_h, and q_h are given as in (38a) and (38b), and after applying the boundary conditions we arrive at the generalized eigenvalue problem

$$\boldsymbol{AU} = k_0^2 \boldsymbol{BU}, \tag{41c}$$

where the matrices $\boldsymbol{A}$ and $\boldsymbol{B}$ represent the left-hand and right-hand sides of the system (41a) and (41b), respectively, and $\boldsymbol{U}$ is a vector collecting all unknown degrees of freedom.

As an example, we consider a problem seeking the *TE* modes that can exist in a circular cavity (the cross-section of a circular waveguide). In these modes (transverse electric, or *TE*), the electric field vector is entirely contained in the cross-section [51,60], and here we can compare the analytical and meshfree solutions in order to study the convergence rate.

When integrating the weak forms, we employ the 2×2 Gauss integration rule with $n_{sub} = 4$ (a coarser scheme) and also with $n_{sub} = 6$ (a finer scheme). We are interested in the TE_{01} mode, and measure the relative error in the L^2 norm given by:

$$\epsilon = \sqrt{\int_\Omega |\boldsymbol{E}_h - \boldsymbol{E}_{01}|^2 d\Omega} \Big/ \sqrt{\int_\Omega |\boldsymbol{E}_{01}|^2 d\Omega}, \tag{42}$$

which is a function of the discretization length h. Fig. 3 shows the result, and that the convergence rates are $\epsilon(h) = C_1 h^{0.878}$ and $\epsilon(h) = C_2 h^{0.886}$, for the $n_{sub} = 4$ and $n_{sub} = 6$ rules, respectively, where C_1 and C_2 are positive constants.

We also solve (40a)–(40c) using standard Nédélec CT/LN (constant-tangential/linear-normal) vector basis elements (i.e., using edge elements) [43]. The convergence rate for the error of these solutions (Fig. 3) is given as $\epsilon(h) = C_3 h^{1.063}$. However, the finite element solution based on the edge elements returns many eigenfunctions associated with the zero eigenvalue (the gradient fields) [43,61], which represents a waste of computational power. This effect is not seen in the meshfree formulation developed here and in other finite element formulations, such as [46].

6.2. Scattering by a PEC circular cylinder

We consider next a plane wave $\boldsymbol{E}^{inc.}(\boldsymbol{x}) = \boldsymbol{E}^{inc.}(x_1, x_2) = e^{-jk_0 x_1}\hat{\boldsymbol{x}}_2$, in V/m, where $k_0 = 24\pi\ \mathrm{m}^{-1}$, propagating onto a cylinder (see Fig. 4). We shall find the two components of the scattered field $\boldsymbol{E}_h^s = [E_{h,1}^s, E_{h,2}^s]^T$ in the x_1x_2 plane. Consider the closed square region $\Pi = [-L, L] \times [-L, L]$ as in (4a), where $L = 6\lambda_0$ (the wavelength λ_0 is related to k_0 by $k_0 = 2\pi/\lambda_0$). Consider also a circle Σ whose radius

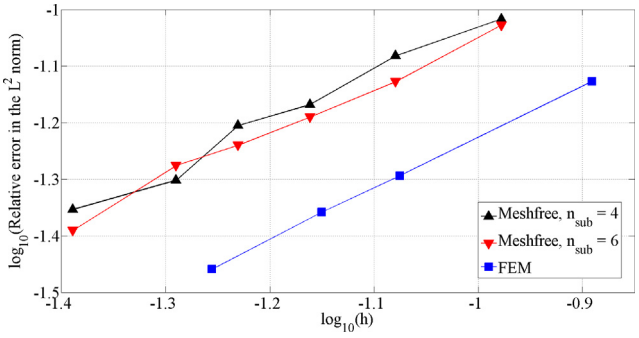

Fig. 3. Relative error for the TE_{01} mode in the circular cavity problem, calculated according to (42).

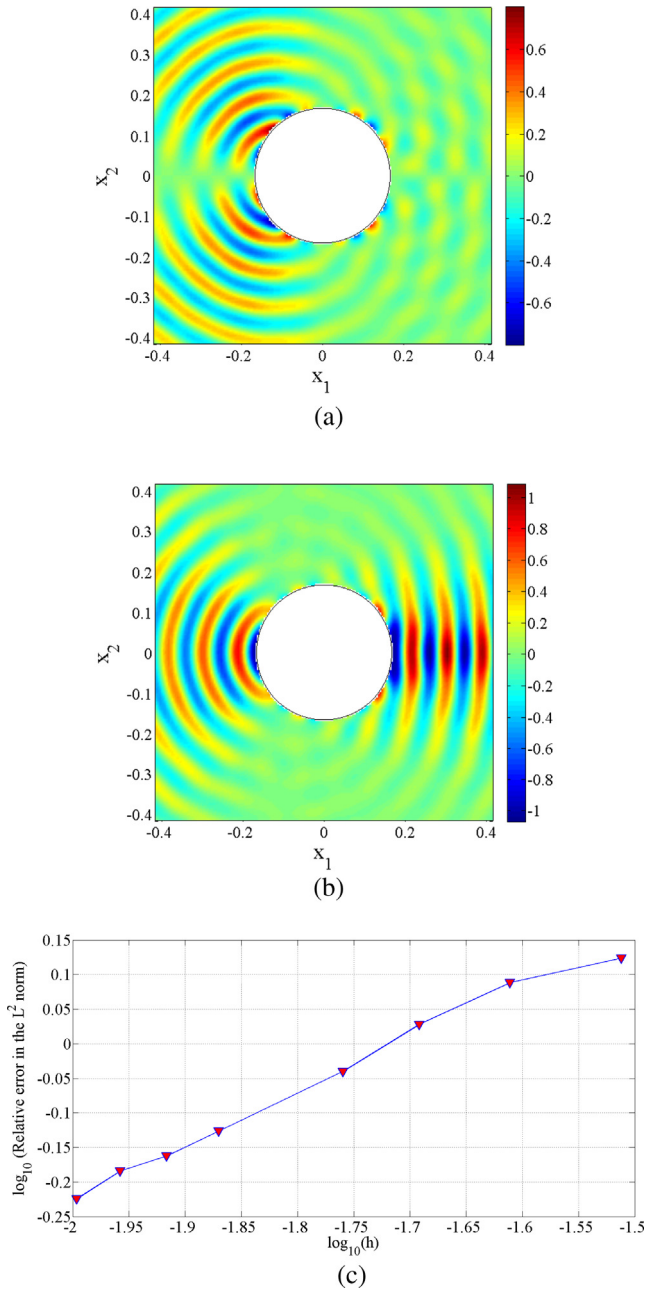

Fig. 4. The scattered electric field $\boldsymbol{E}_h^s$, in V/m, in the cylinder problem. The coordinates x_1 and x_2 are measured in meters. (a) The real part of $E_{h,1}^s$ (component 1). (b) Real part of $E_{h,2}^s$ (component 2). (c) Relative error calculated according to (43).

$a = 2\lambda_0$, i.e., $\Sigma = \{\boldsymbol{x} \in \mathbb{R}^2 : \|\boldsymbol{x}\|^2 \leqslant a^2\}$. For the width of the PML, we use $w_{PML} = \lambda_0$, and when integrating the weak forms, we employ the 2×2 Gauss integration rule with each element subdivided using $n_{sub} = 6$.

This problem admits an analytical solution $\boldsymbol{E}_{an}^s$ in terms of a series of Hankel functions [51,60], against which we can compare the meshfree solutions calculating the relative error ϵ in the L^2 norm:

$$\epsilon = \sqrt{\int_{\Omega - \Omega_{PML}} |\boldsymbol{E}_h^s - \boldsymbol{E}_{an}^s|^2 d\Omega} \Big/ \sqrt{\int_{\Omega - \Omega_{PML}} |\boldsymbol{E}_{an}^s|^2 d\Omega}, \tag{43}$$

where the region Ω_{PML} occupied by the PML is excluded from the calculations. The solutions in Fig. 4 have been obtained using 9,192 nodes with a total of 61,656 unknown coefficients. To obtain

the error as a function of h, we vary h and obtain Fig. 4c. A linear regression reveals that $\epsilon(h) = C_1 h^{0.7641}$, where C_1 is a positive constant.

6.3. Scattering by a conducting strip

Here we consider the problem regarding the scattering of a TE_z plane wave (transverse electric to x_3, or z) by a conducting strip (see Fig. 5a). Assume that $k_0 = 40\pi\ \mathrm{m}^{-1}$, and let $\Pi = [-7\lambda_0, 13\lambda_0] \times [-10\lambda_0, 10\lambda_0]$ be a square region. A zero-thickness strip Σ of width $b = 6\lambda_0$ is placed at the center of Π, i.e., $\Sigma = \{\boldsymbol{x} \in \mathbb{R}^2 : 0 \leqslant x_1 \leqslant 6\lambda_0, x_2 = 0\}$. The PML width is $w_{PML} = 4\lambda_0$. The incident magnetic field is given by $\boldsymbol{H}^{inc.}(\boldsymbol{x}) = H_0 e^{-jk_0 \widehat{\boldsymbol{k}}\cdot\boldsymbol{x}} \widehat{\boldsymbol{x}}_3$, where $H_0 = 1$ A/m. Moreover, $\widehat{\boldsymbol{k}} = [k_1, k_2]^T$ is the unit vector pointing in the direction of propagation of the incident plane wave, where $\widehat{\boldsymbol{k}} = [-\cos\varphi_i, -\sin\varphi_i]^T$ and φ_i is the *incidence angle* (a polar angle with respect to the origin of the coordinate system, as in Fig. 5a). The incident electric field is recovered from Ampére's law in free space $\nabla \times \boldsymbol{H}^{inc.} = j\omega\varepsilon_0 \boldsymbol{E}^{inc.}$:

$$\boldsymbol{E}^{inc.}(\boldsymbol{x}) = -\eta_0 H_0 (k_2 \widehat{\boldsymbol{x}}_1 - k_1 \widehat{\boldsymbol{x}}_2) e^{-jk_0 \widehat{\boldsymbol{k}}\cdot\boldsymbol{x}}, \tag{44}$$

where $\eta_0 = 120\pi$ is the *vacuum impedance* (in ohms). The incidence angle is chosen to be $\varphi_i = 2\pi/3$. We use a regular nodal distribution and $n_{sub} = 6$ with 2×2 Gauss integration. Our discretization uses 10,201 nodes, with 68,917 unknown solution variables. The components 1 and 2 of the predicted scattered electric field $\boldsymbol{E}^s_h = [E^s_{h,1}, E^s_{h,2}]^T$ are plotted in Fig. 5b and c, respectively.

Not having an analytical solution, we validate the results using the electric field integral equation with the method of moments (MoM) [43]. The results are given in Fig. 5d, which shows a good correspondence between the near-field solutions provided by both methods.

6.4. Modes of a spherical cavity

This problem is the three-dimensional counterpart of the problem in Section 6.1. We consider the domain Ω to be a unit sphere representing a hollow spherical cavity bounded by conducting walls (see Figs. 6–9). Our objective with this example solution is to establish if the meshfree spaces are appropriate when used in the solution of problems with three-dimensional curvilinear geometries. Fig. 6 illustrates some nodes scattered on the spherical surface $\partial\Omega$. For each node I located on $\partial\Omega$, the three unit basis vectors $\{\boldsymbol{\sigma}^I_1, \boldsymbol{\sigma}^I_2, \boldsymbol{\sigma}^I_3\}$, also seen in Fig. 6, are determined as discussed above.

The eigenfunctions of the spherical cavity have analytical expressions [51,60]. In spherical coordinates (r, θ, φ), and for the TM_r (transverse magnetic to r) modes, the r component of the magnetic vector potential $\boldsymbol{A}$ is expressed as a product of three terms:

$$A_r = \alpha \hat{J}_n\left(\frac{\zeta'_{np}}{a} r\right) P^m_n(\cos\theta)[C\cos(m\varphi) + D\sin(m\varphi)], \tag{45a}$$

where α is a (normalization) constant, $\hat{J}_n$ are the Schelkunoff-Bessel functions of the first kind and order n, a is the radius of the sphere, and the P^m_n are the associated Legendre polynomials of the first kind [51]. Each eigenvalue is determined by two indices n and p, and ζ'_{np} is the p -th zero of the derivative of the Schelkunoff-Bessel function $\hat{J}_n$. Therefore each mode is characterized by n, p, and m, and displays either *even* or *odd* symmetry with respect to the azimuthal angle φ.

We limit our solution to just two modes. Their labeling indices $\{n, p, m, symmetry\}$ are $\{1, 1, 0, even\}$ and $\{2, 1, 1, odd\}$. Expression (45a) allows us to find the spherical components E_r, E_θ, and E_φ of the electric field [51], from which we obtain the field in Cartesian coordinates E_1, E_2, and E_3. These form the analytical description of the fields $\boldsymbol{E}_{110,even}$ and $\boldsymbol{E}_{211,odd}$. The meshfree solutions are calculated from (41a)–(41c), where we employ $2 \times 2 \times 2$ Gauss integra-

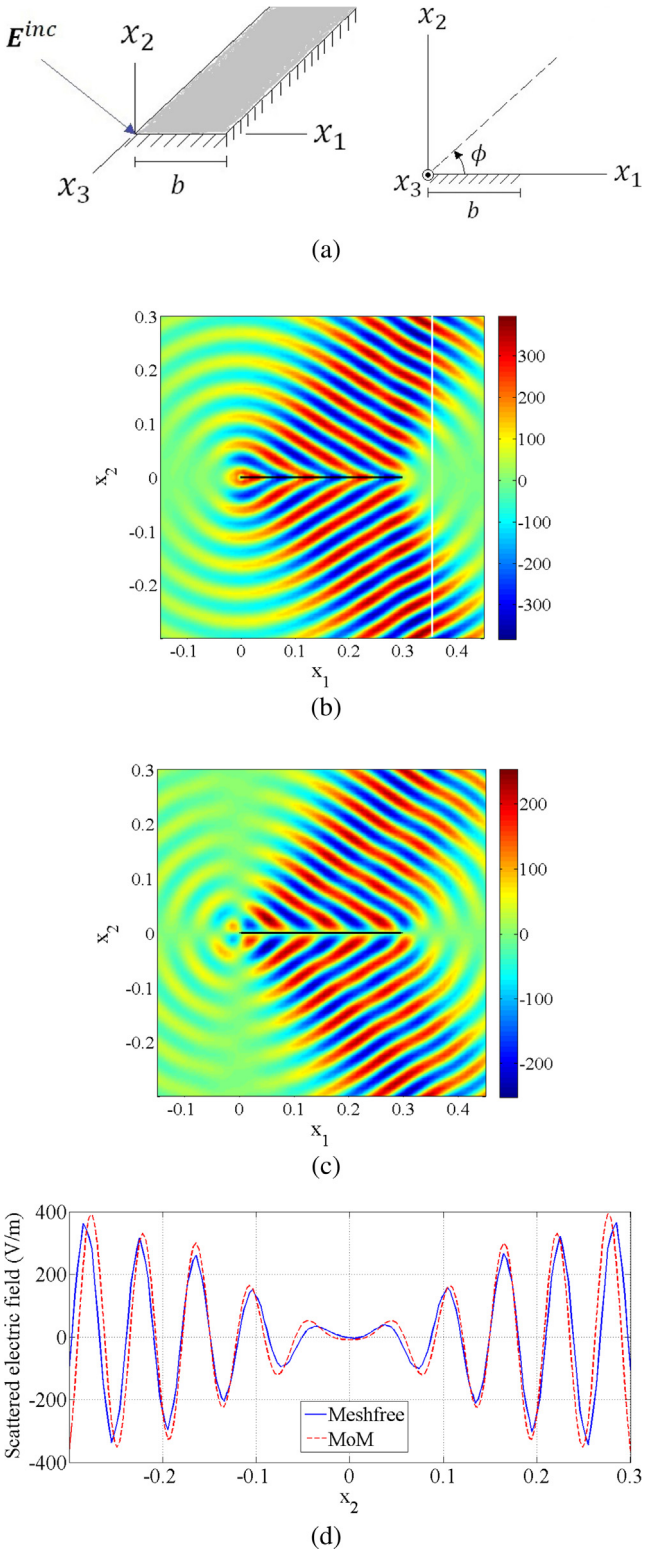

Fig. 5. The strip problem. (a) The conducting strip extends to infinity along the x_3 (or z) direction. In the x_1x_2 (or xy) plane, we can set up the standard polar system of coordinates. In this way, the incidence angle φ_i is measured as in the figure. The coordinates x_1 and x_2 are measured in meters. (b) The real part of $E^s_{h,1}$ (component 1), in V/m. (c) Real part of $E^s_{h,2}$ (component 2), in V/m. (d) Real part of $E^s_{h,1}$ along the path $x_1 = 0.35$, $-0.3 \leqslant x_2 \leqslant 0.3$, shown as a vertical white line in Fig. 5b. The meshfree and MoM solutions are shown in the figure.

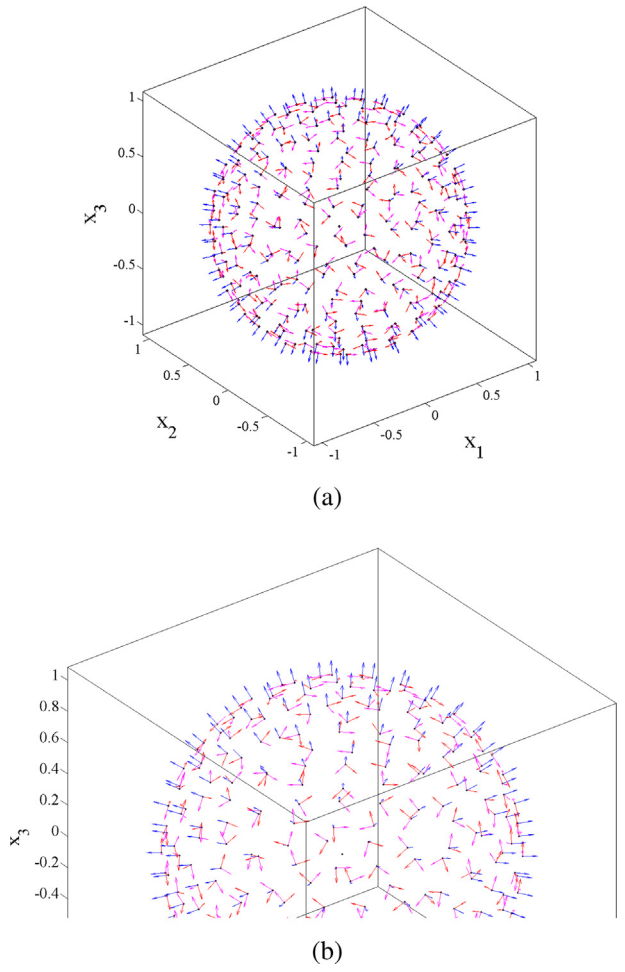

Fig. 6. Nodes distributed over the surface $\partial\Omega$ of the sphere. (a) Corresponding to each node I on $\partial\Omega$, there is a set of three mutually orthogonal unit vectors $\{\boldsymbol{\sigma}_1^I, \boldsymbol{\sigma}_2^I, \boldsymbol{\sigma}_3^I\}$, determined as in Section 3.4. (b) A zoom is applied.

tion for each element subdivided with $n_{sub} = 6$. The Cartesian components $E_{h,i}$, $i = 1, 2, 3$ are determined from the scalar product between $\boldsymbol{E}_h$ (which admits an expansion as in (38a)) and the unit vectors $\widehat{\boldsymbol{x}}_i$, i.e., for any point $\boldsymbol{x}$ in $\overline{\Omega}$,

$$E_{h,i}(\boldsymbol{x}) = \boldsymbol{E}_h(\boldsymbol{x}) \cdot \widehat{\boldsymbol{x}}_i = \sum_{I=1}^{N} \sum_{m=1}^{d+1} \sum_{k=1}^{d} h_{Im}(\boldsymbol{x}) \boldsymbol{\sigma}_k^I \cdot \widehat{\boldsymbol{x}}_i \widetilde{E}_{Im}^k. \tag{45b}$$

The results for the modes $\boldsymbol{E}_{110,even}$ and $\boldsymbol{E}_{211,odd}$ calculated at the surface of the sphere are plotted in Figs. 7 and 8, respectively. We also vary h and calculate the relative error in the L^2 norm for the mode $\{1, 1, 0, even\}$. The result is shown in Fig. 9, which reveals a convergence rate $\epsilon(h) = C_1 h^{1.138}$, where C_1 is a positive constant.

6.5. Scattering by conducting plates

Consider now the three-dimensional scattering of plane waves by rectangular PEC plates (see Figs. 10–12). Let $k_0 = 18\pi\ \mathrm{m}^{-1}$, and let Π be defined as:

$$\Pi = [-4.5\lambda_0, 4.5\lambda_0] \times [-4.5\lambda_0, 4.5\lambda_0] \times [-1.5\lambda_0, 1.5\lambda_0]. \tag{46a}$$

We assume a zero-thickness plate of width $6\lambda_0$ placed symmetrically at the center of Π:

$$\Sigma = \{\boldsymbol{x} \in \mathbb{R}^3 : -3\lambda_0 \leqslant x_1 \leqslant 3\lambda_0, \quad -3\lambda_0 \leqslant x_2 \leqslant 3\lambda_0, x_3 = 0\}. \tag{46b}$$

The PML width is chosen as $w_{PML} = 0.75\lambda_0$.

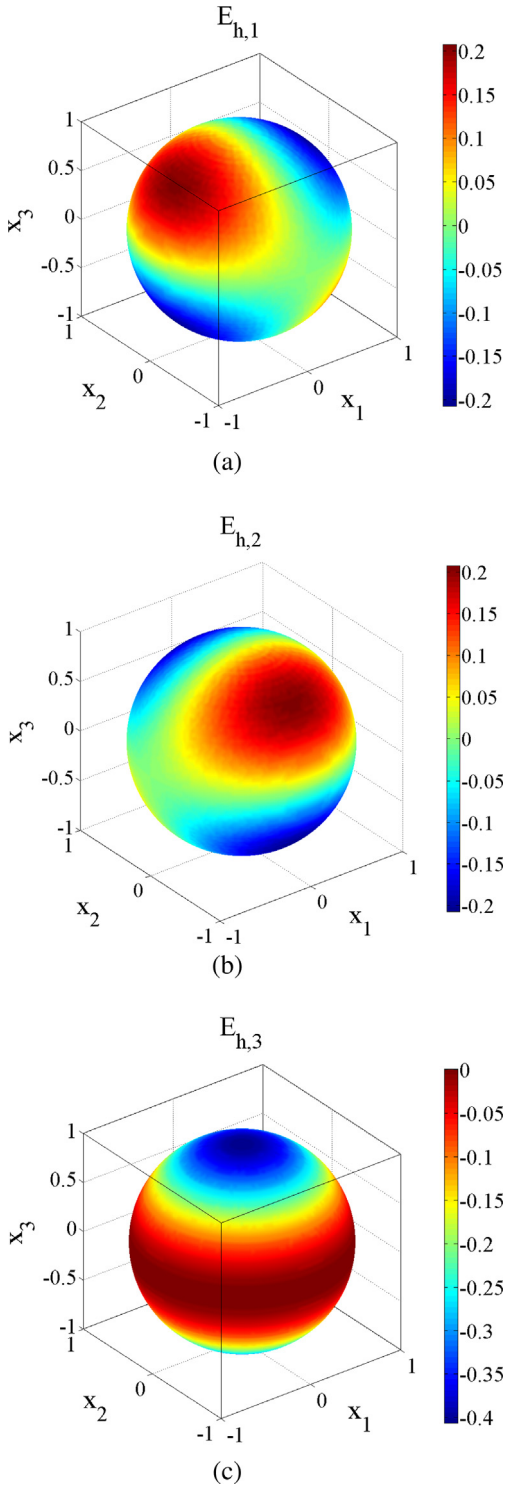

Fig. 7. Cartesian components of the eigenmode $\{1, 1, 0, even\}$. (a) Component $E_{h,1}$. (b) Component $E_{h,2}$. (c) Component $E_{h,3}$.

In the spherical coordinate system (r, θ, φ) (as in Fig. 10a), given the *incidence angles* θ_i and φ_i, the direction of propagation of the incident plane wave is given by

$$\widehat{\boldsymbol{k}} = \begin{bmatrix} k_1 \\ k_2 \\ k_3 \end{bmatrix} = \begin{bmatrix} -\sin\theta_i \cos\varphi_i \\ -\sin\theta_i \sin\varphi_i \\ -\cos\theta_i \end{bmatrix}. \tag{46c}$$

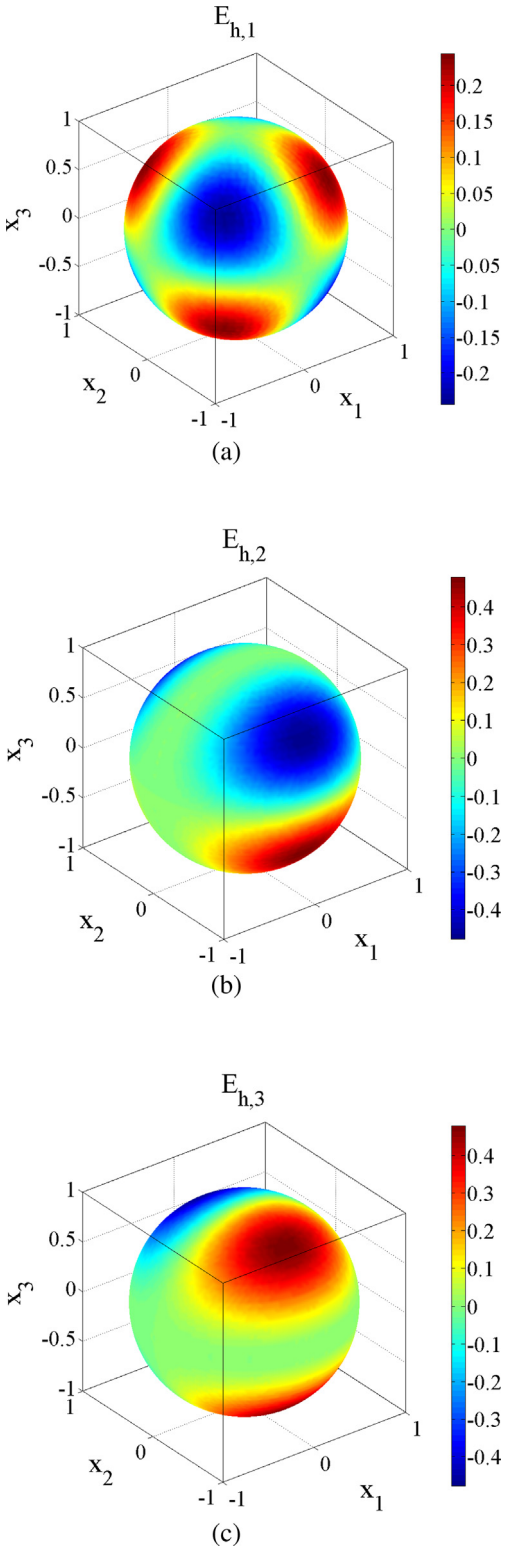

Fig. 8. Cartesian components of the eigenmode $\{2,1,1,odd\}$. (a) Component $E_{h,1}$. (b) Component $E_{h,2}$. (c) Component $E_{h,3}$.

In this example, we consider two polarizations for the incident plane wave. The first, called TM_x (transverse magnetic to x_1, or x), is characterized by an incident electric field given by

$$\boldsymbol{E}^{inc.}(\boldsymbol{x}) = E_0 e^{-jk_0 \widehat{\boldsymbol{k}\cdot\boldsymbol{x}}} \widehat{\boldsymbol{x}}_1, \tag{46d}$$

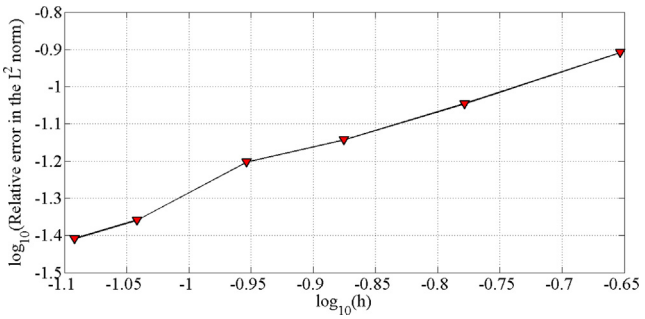

Fig. 9. Relative error for the eigenmode $\{1,1,0,even\}$ in the spherical cavity problem.

where $E_0 = 1$ V/m. The second, called TE_x (transverse electric to x_1, or x), is characterized by an incident magnetic field given by $\boldsymbol{H}^{inc.}(\boldsymbol{x}) = H_0 e^{-jk_0 \widehat{\boldsymbol{k}\cdot\boldsymbol{x}}} \widehat{\boldsymbol{x}}_1$, where $H_0 = 1$ A/m. Application of Ampère's law shows that the associated incident electric field for this polarization is

$$\boldsymbol{E}^{inc.}(\boldsymbol{x}) = -\eta_0 H_0 (k_3 \widehat{\boldsymbol{x}}_2 - k_2 \widehat{\boldsymbol{x}}_3) e^{-jk_0 \widehat{\boldsymbol{k}\cdot\boldsymbol{x}}}. \tag{46e}$$

In the TM_x problem, we choose $(\theta_i, \varphi_i) = (\pi/4, 3\pi/2)$. A uniform nodal cloud of 27,735 nodes is used, which originates 307,667 degrees of freedom. For the integration of the weak forms, we use the $2 \times 2 \times 2$ Gauss rule, with $n_{sub} = 6$ for each element. We consider a box placed $0.375\lambda_0$ away from the plate, i.e., the box B given by:

$$\begin{aligned} B = \{\boldsymbol{x} \in \mathbb{R}^3 : &-3.375\lambda_0 \leqslant x_1 \leqslant 3.375\lambda_0, \\ &-3.375\lambda_0 \leqslant x_2 \leqslant 3.375\lambda_0, \\ &-0.375\lambda_0 \leqslant x_3 \leqslant 0.375\lambda_0\}, \end{aligned} \tag{46f}$$

which completely encloses the plate. The three Cartesian components $E^s_{h,1}, E^s_{h,2}, E^s_{h,3}$ of the scattered field are calculated on the surface ∂B of the box B in (46f) and displayed in Fig. 10. For the TE_x problem, we choose $(\theta_i, \varphi_i) = (\pi/6, 3\pi/2)$, and the same nodal distribution and integration rule as for the TM_x problem are employed. The Cartesian components of the scattered field are again calculated on ∂B and displayed in Fig. 11.

These problems do not admit analytical solutions. To validate the numerical solutions, we focus on the *far-field* pattern. At each point of the surface ∂B, we can calculate the scattered electric field $\boldsymbol{E}^s_h$, and also the scattered magnetic field, given by Faraday's law $\nabla \times \boldsymbol{E}^s_h = -j\omega\mu_0 \boldsymbol{H}^s_h$. Using the surface equivalence principle [51], $\boldsymbol{E}^s_h$ and $\boldsymbol{H}^s_h$ produce 'equivalent' surface current densities on ∂B given by

$$\boldsymbol{J}_{eq} = \widehat{\boldsymbol{n}} \times \boldsymbol{H}^s_h, \tag{46g}$$

$$\boldsymbol{M}_{eq} = -\widehat{\boldsymbol{n}} \times \boldsymbol{E}^s_h,$$

where $\boldsymbol{J}_{eq}$ and $\boldsymbol{M}_{eq}$ are the equivalent electric and magnetic surface current densities, respectively, and $\widehat{\boldsymbol{n}}$ is a unit vector normal to ∂B. The field $\boldsymbol{E}^s$ at a distance from the plate can be determined using suitable radiation integrals [51]. These depend on $\boldsymbol{J}_{eq}$ and $\boldsymbol{M}_{eq}$, and are evaluated over ∂B. The fields at infinity can be determined through a *far-field approximation* and the *radar cross-section* (RCS) can be calculated [43,51]:

$$\sigma_{3D}(\theta_s, \varphi_s) = \lim_{r_s \to \infty} 4\pi r_s^2 \frac{|\boldsymbol{E}^s(r_s, \theta_s, \varphi_s)|^2}{|\boldsymbol{E}^{inc}|^2}, \tag{46h}$$

We consider a set of observation angles (θ_s, φ_s) and for each one of these determine the *normalized* radar cross-section given by σ_{3D}/λ_0^2, i.e., σ_{3D} divided by the square of the wavelength $\lambda_0 = 2\pi/k_0$ [51,62].

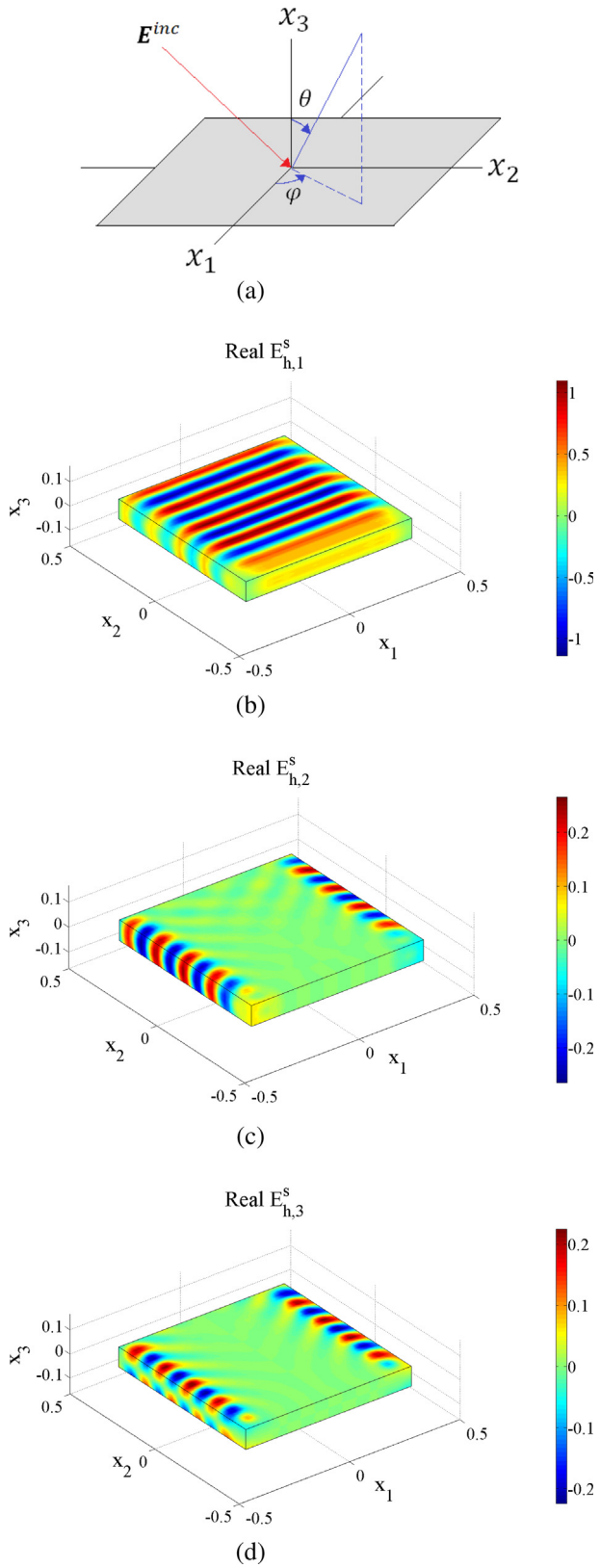

Fig. 10. Scattering by plates. (a) Geometry of the scattering system. We can set up the standard spherical coordinate system, so that any direction can be identified by the pair of angles (θ, φ). The incident field $\boldsymbol{E}^{inc.}$ has its direction determined by (θ_i, φ_i). (b) TM_x polarization, real part of $E^s_{h,1}$ over the surface of the box B in (46f), in V/m. (c) Real part of $E^s_{h,2}$. (d) Real part of $E^s_{h,3}$. Dimensions x_1, x_2, x_3 in meters.

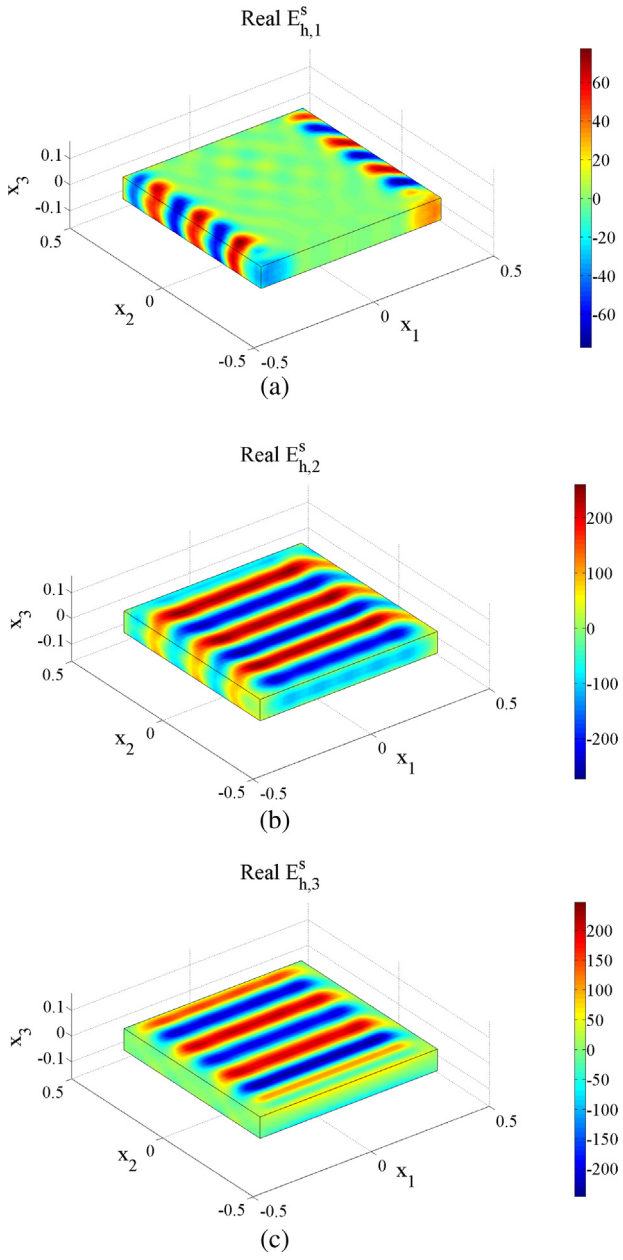

Fig. 11. The plate problem, TE_x polarization. (a) Real part of $E^s_{h,1}$ over the surface of the box B in (46f), in V/m. (b) Real part of component $E^s_{h,2}$. (c) Real part of $E^s_{h,3}$. Dimensions x_1, x_2, x_3 in meters.

Having calculated the radar cross-section for a given set of observation angles, we compare our results with the Physical Optics closed form approximation [51,63,64]. The Physical Optics approximation is most accurate when compared with the 'full field theory' solution in the *specular direction*, i.e., the direction along which the incident wave is reflected by the conducting surface, in a ray tracing approach. The predictions of the Physical Optics become less accurate away from the specular directions. One of the reasons is that the Physical Optics approximation fails to take edge diffractions into account [51].

The normalized RCS provided by our meshfree method and by the Physical Optics approximation are plotted in Fig. 12, which gives results in *decibels*, i.e., as $10\log_{10}(\sigma_{3D}/\lambda_0^2)$. They are seen to agree with each other in the vicinity of the specular directions.

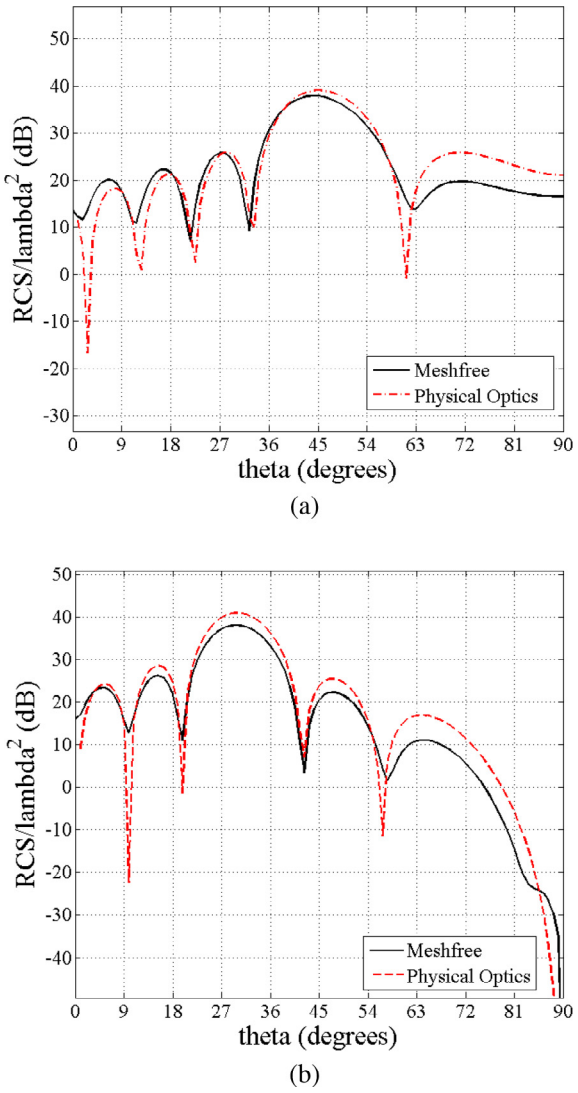

Fig. 12. Radar cross-sections. (a) Normalized radar cross-section (RCS) in decibels for the 3D scattering of a TM_x plane wave by a PEC plate. (b) Normalized RCS in decibels for the scattering of a TE_x plane wave by a PEC plate. In these figures, the RCS is calculated for the observation angles $\varphi_s = 90^\circ$ and $0 \leqslant \theta_s \leqslant 90^\circ$. The RCS calculated from the meshfree solutions are compared with those predicted by the Physical Optics. The Physical Optics is an approximation, whose predictions agree with those of the 'full' field theory only in the vicinity of the specular directions, given by 45° in (a) and 30° in (b).

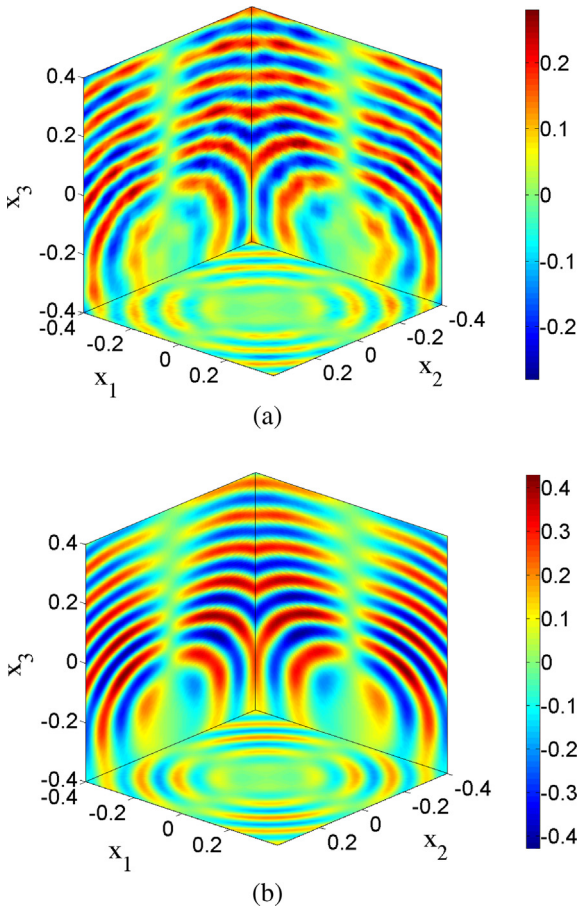

Fig. 13. The real part of component 2 of the scattered electric field (in V/m) plotted over the surface of the cubic box $B = [-4\lambda_0, 4\lambda_0]^3$. The plane $x_3 = -0.4$ touches the south pole of the conducting sphere. (a) A relatively coarse meshfree solution. (b) Analytical solution. Dimensions x_1, x_2, x_3 in meters.

6.6. Scattering by a conducting sphere

The purpose of this section is to examine the number of unknowns required when using the proposed solution scheme. The analysis constitutes a preliminary consideration about the ability of the method to be extended and applied to larger problems in engineering.

Consider $k_0 = 20\pi\ \mathrm{m}^{-1}$, and let Π be a cubic box defined as $\Pi = [-6\lambda_0, 6\lambda_0]^3$. The set which represents the conducting sphere is $\Sigma = \{\boldsymbol{x} \in \mathbb{R}^3 : \|\boldsymbol{x}\|^2 \leqslant a^2\}$, where $a = 4\lambda_0$. The incident electric field is $\boldsymbol{E}^{inc.}(\boldsymbol{x}) = E_0 e^{-jk_0 \widehat{\boldsymbol{k}}\cdot\boldsymbol{x}} \widehat{\boldsymbol{x}}_1$, where $E_0 = 1\ \mathrm{V/m}$ and $\widehat{\boldsymbol{k}} = [0, 0, 1]^T$, i.e., the plane wave propagates from south to north. The width of the PML is $w_{PML} = \lambda_0$. As for the nodal cloud, we employ a regular distribution in the central portion of the domain Ω, and a non-regular distribution on and close to the spherical boundary $\partial\Sigma$. When integrating the weak forms, we use a 1-point Gauss rule, and subdivide the patches according to $n_{sub} = 12$ for the nodes in the central portions and $n_{sub} = 8$ for the nodes on and close to $\partial\Sigma$.

The Cartesian component $E^s_{h,2}$ of the scattered field is plotted on the surface ∂B of the cubic box $B = [-4\lambda_0, 4\lambda_0]^3$ in Fig. 13a. The analytical solution [51,60] is plotted in Fig. 13b. There is a reasonable agreement between the numerical and analytical solutions, and the quality of the results can be improved by increasing the number of nodes.

In the solution of this problem, a relatively small number of nodes has been used. Our cloud has 79,883 nodes, which produces 894,991 unknowns. The side of the box Π is $12\lambda_0$, so that its volume is $1,728\ \lambda_0^3$. The radius of the sphere is $a = 4\lambda_0$, and its volume is given by $4\pi a^3/3$, which amounts to approximately $268\ \lambda_0^3$. Therefore, the volume of the computational domain Ω is $1,460\ \lambda_0^3$. We now define the *density of unknowns* $\mathcal{D}_{unk}$ as the number of unknowns N_{unk} divided by the volume of the computational domain (in cubic wavelengths) and obtain:

$$\mathcal{D}_{unk} := \frac{N_{unk}}{\mathrm{vol}(\Omega)} = \frac{894,991}{1,460\lambda_0^3} \cong 613 \frac{\text{unknowns}}{\lambda_0^3}. \tag{47a}$$

This result tells that about 9 unknowns are needed per wavelength (when assumed to propagate in each direction) to capture the wave, which is quite reasonable.

From this preliminary analysis it can be seen that we can use the proposed method to obtain reasonable results with a relatively low number of unknowns. However, the total computational effort is given by the numerical integrations and by the solution of the

governing equations, and we have not focused as yet on these aspects of the solution.

7. Concluding remarks

In this paper we presented a new scheme for the solution of electromagnetic wave scattering problems from conducting targets. The scheme can be used when curved geometries are considered.

Since the electric field associated with the scattered wave is a vector quantity constrained by a divergence-free condition, we introduced a Lagrange multiplier, arriving at a mixed formulation. It follows that the discretization scheme must employ different spaces for approximating the solution variables and an inf-sup condition must be satisfied. The formulation resembles that used to solve the Navier-Stokes fluid flows.

The results we obtained agree with analytical solutions and with those provided by other techniques. Hence the method developed here is a promising scheme for the solution of electromagnetic wave scattering problems in domains of complex geometry.

However, while we have presented the scheme and illustrative solutions, we did not focus on the computational effort required in the numerical integration (to establish the governing matrix and vector) and in the solution of the governing equations. This computational effort should be assessed in detail in comparison to the use of other schemes. To reduce the numerical integration effort, the procedures proposed in [3] provide an effective avenue, and have already shown a good promise in the solutions of some structural analysis problems [3].

Future work might consider using the scheme, indeed an extension thereof, to solve electric field problems that include different media and singularities, as widely encountered in electromagnetics. Also, an extension of the technique to solve more complex problems would be valuable, e.g., problems with dielectric (penetrable) objects, or with magnetic materials, such as ferrites, and also fully coupled problems of multi-physics phenomena [46].

Acknowledgments

This work was supported by the State of Minas Gerais, Brazil (FAPEMIG), in the form of the grants TEC-22019/12 and TEC-APQ-00667/12, and by the Brazilian Ministry of Education (CAPES), PROCAD project 88881.068419/2014-01.

Appendix A

The conditions for well-posedness of Eqs. (37) are a classical result used in the study of mixed finite element formulations with real-valued bilinear forms (see for example [48,49,55,57,65]). While the formulation to solve scattering problems proposed in this paper uses complex-valued forms, it can be shown using the techniques from the aforementioned references and from [53,54] that an inf-sup condition evaluated for spaces of real-valued functions implies the surjectivity of the operator B associated with the sesquilinear form b in (36d), as required by the theory (see for example Section 2.1.1 in [49] and Section 6.12 in [54]).

In this appendix, we quote this inf-sup condition and only focus on its verification for the proposed discretization scheme.

A.1. The discrete inf-sup condition

From (31b) and (31c), arbitrary elements from $\mathbb{V}_h$ and $\mathbb{P}_h$ admit expansions in terms of real-valued meshfree basis functions and complex coefficients. We introduce the spaces of real-valued functions $\mathbb{V}_h[\mathbb{R}]$ and $\mathbb{P}_h[\mathbb{R}]$:

$$\boldsymbol{v}_h \in \mathbb{V}_h[\mathbb{R}] \iff \begin{cases} \boldsymbol{v}_h = \sum_{lmk} h_{lm} \boldsymbol{\sigma}_k^l \tilde{v}_{lm}^k, \\ \tilde{v}_{lm}^k \in \mathbb{R}, \\ \widehat{\boldsymbol{n}} \times \boldsymbol{v}_h|_{\partial\Omega} = \boldsymbol{0}, \end{cases} \tag{A.1}$$

$$q_h \in \mathbb{P}_h[\mathbb{R}] \iff \begin{cases} q_h = \sum_{l=1}^{N} \varphi_l \tilde{q}_l, \\ \tilde{q}_l \in \mathbb{R}, \end{cases} \tag{A.2}$$

The inf-sup condition to be satisfied by the discrete meshfree spaces is:

There exists a constant $\gamma_h > 0$ such that

$$\inf_{q_h \in \mathcal{P}} \sup_{\boldsymbol{v}_h \in \boldsymbol{\mathcal{V}}} \frac{\int_\Omega q_h \nabla \cdot \boldsymbol{v}_h d\omega}{\|q_h\|_{\mathbb{P}_h[\mathbb{R}]} \|\boldsymbol{v}_h\|_{\mathbb{V}_h[\mathbb{R}]}} \geqslant \gamma_h, \tag{A.3}$$

where $\boldsymbol{\mathcal{V}} = \mathbb{V}_h[\mathbb{R}] - \{\boldsymbol{0}\}$ and $\mathcal{P} = \mathbb{P}_h[\mathbb{R}] - \{0\}$. This result is a consequence of the Banach Closed Range and Open Mapping Theorems (see, for example, [49,53,54]). It can be shown that (A.3), which involves the real spaces $\mathbb{V}_h[\mathbb{R}]$ and $\mathbb{P}_h[\mathbb{R}]$, is one of the conditions assuring the well-posedness of the discrete problem (37), which involves the complex spaces $\mathbb{V}_h$ and $\mathbb{P}_h$. In (A.3), the norm $\|\cdot\|_{\mathbb{V}_h[\mathbb{R}]}$ is the (vector) H^1 norm [54], and $\|\cdot\|_{\mathbb{P}_h[\mathbb{R}]}$ is the (scalar) L^2 norm [54]. The reason is that $\mathbb{V}_h$ and $\mathbb{P}_h$ are subspaces of $H^1(\Omega;\mathbb{C})^d$ and $L^2(\Omega;\mathbb{C})$, respectively.

A.2. The inf-sup test

The goal of this section is to study the inf-sup condition (A.3). It should be pointed out that in the context of mixed finite elements, proving that a pair of discrete spaces satisfies an appropriate inf-sup condition is a very difficult task. Some pairs that do satisfy the condition are documented in the literature [48]. However, one could in principle be interested in a new pair of discrete spaces and not be able to find a formal proof that it satisfies the inf-sup condition.

In order to overcome this difficulty, a numerical test has been proposed for testing if a given pair of finite element spaces satisfies an appropriate inf-sup condition [66–69]. In this way, the inf-sup condition is not actually proved, but verified experimentally.

The test has found much success [48,70], and has also been used in a two-dimensional meshfree solution in computational mechanics [50]. We apply it here to the proposed solution scheme for electromagnetic wave scattering.

Consider a test domain Ω, which could be a square in 2D [50] or a cube in 3D. Introduce the matrices $\boldsymbol{B}$, $\boldsymbol{S}_{\mathbb{V}}$, and $\boldsymbol{S}_{\mathbb{P}}$, which are matrix representations of the following operations:

$$\int_\Omega q_h \nabla \cdot \boldsymbol{v}_h d\Omega, \tag{A.4}$$

$$(\boldsymbol{w}_h, \boldsymbol{v}_h)_{\mathbb{V}_h[\mathbb{R}]} = \int_\Omega (\boldsymbol{w}_h \cdot \boldsymbol{v}_h + \nabla \boldsymbol{w}_h : \nabla \boldsymbol{v}_h) d\Omega, \tag{A.5}$$

$$(q_h, t_h)_{\mathbb{P}_h[\mathbb{R}]} = \int_\Omega q_h t_h d\Omega. \tag{A.6}$$

By 'matrix representation', we mean that expanding q_h as in (A.2) and $\boldsymbol{v}_h$ as in (A.1), and collecting all degrees of freedom $\tilde{q}_l$ into a vector $\widetilde{\boldsymbol{Q}}$ whose size is $\dim \mathbb{P}_h[\mathbb{R}] \times 1$, and all degrees of freedom $\tilde{v}_{lm}^k$ into a vector $\widetilde{\boldsymbol{V}}$ whose size is $\dim \mathbb{V}_h[\mathbb{R}] \times 1$, then (A.4) is expressed as:

$$\int_\Omega q_h \nabla \cdot \boldsymbol{v}_h d\Omega = \widetilde{\boldsymbol{Q}}^T \boldsymbol{B} \widetilde{\boldsymbol{V}}, \tag{A.7}$$

from which it is clear that the size of the matrix $\boldsymbol{B}$ is $\dim \mathbb{P}_h[\mathbb{R}] \times \dim \mathbb{V}_h[\mathbb{R}]$. Likewise, if $\boldsymbol{w}_h$ is expanded as in (A.1), and t_h is expanded as in (A.2), and if their degrees of freedom $\widetilde{w}_{Im}^k$ and $\tilde{t}_I$ are collected into vectors $\widetilde{\boldsymbol{W}}$ and $\widetilde{\boldsymbol{T}}$, respectively, then (A.5) and (A.6) can be expressed as:

$$\int_\Omega (\boldsymbol{w}_h \cdot \boldsymbol{v}_h + \nabla \boldsymbol{w}_h : \nabla \boldsymbol{v}_h) d\Omega = \widetilde{\boldsymbol{W}}^T \boldsymbol{S}_{\mathbb{V}} \widetilde{\boldsymbol{V}}, \tag{A.8}$$

$$\int_\Omega q_h t_h d\Omega = \widetilde{\boldsymbol{Q}}^T \boldsymbol{S}_{\mathbb{P}} \widetilde{\boldsymbol{T}}, \tag{A.9}$$

where the sizes of the matrices $\boldsymbol{S}_{\mathbb{V}}$ and $\boldsymbol{S}_{\mathbb{P}}$ are $\dim \mathbb{V}_h[\mathbb{R}] \times \dim \mathbb{V}_h[\mathbb{R}]$ and $\dim \mathbb{P}_h[\mathbb{R}] \times \dim \mathbb{P}_h[\mathbb{R}]$, respectively.

The elements from $\mathbb{V}_h[\mathbb{R}]$ represent vectors that have zero tangential components along $\partial\Omega$, according to (A.1). Degrees of freedom of zero value have not been included in the assemblage process in (A.4), (A.5), (A.7), and (A.8).

According to the inf-sup test [48,66,70], it can be proved that the left-hand side of (A.3), the *inf-sup value* $v_{inf-sup}(h)$, is equal to the square root of the smallest eigenvalue λ_i in the problem [48]:

$$\boldsymbol{B}\boldsymbol{S}_{\mathbb{V}}^{-1}\boldsymbol{B}^T \widetilde{\boldsymbol{q}}_i = \lambda_i \boldsymbol{S}_{\mathbb{P}} \widetilde{\boldsymbol{q}}_i, \tag{A.10}$$

i.e., $v_{inf-sup}(h) = \sqrt{\lambda_{\min}}$. In this way, (A.3) becomes:

There exists a constant $\gamma_h > 0$ *such that*

$$\sqrt{\lambda_{\min}} = v_{inf-sup}(h) \geqslant \gamma_h. \tag{A.11}$$

If the inf-sup value is larger than zero, then the pair of discrete spaces $\mathbb{V}_h[\mathbb{R}]$ and $\mathbb{P}_h[\mathbb{R}]$ satisfies (A.3).

In order to check the inf-sup stability, the idea is to construct a sequence $n = 1, 2, 3, \ldots$ of discretizations, from less fine to more fine. In this way, the number of nodes N is strictly increasing (i.e., $N_1 < N_2 < N_3 < \cdots$), and the discretization length h is strictly decreasing (i.e., $h_1 > h_2 > h_3 > \cdots$). For each discretization in the sequence, the eigenproblem (A.11) must be solved. Then we obtain a sequence of inf-sup values $v_{inf-sup}(h_n)$ and, for the test to be passed, the values in this sequence should stabilize at a value γ larger than zero, i.e.,

$$\inf\{v_{inf-sup}(h_n) : n \in \mathbb{N}\} = \gamma > 0. \tag{A.12}$$

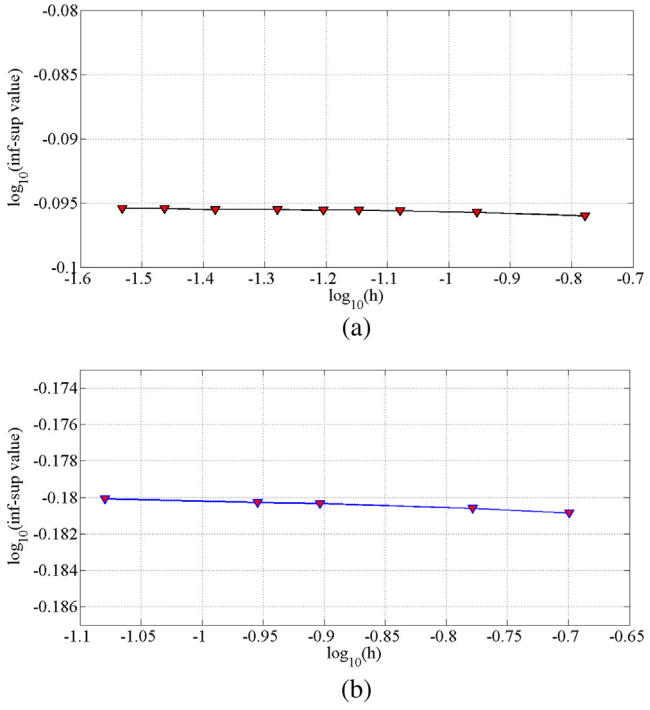

Fig. 14. The inf-sup test. Successive inf-sup values $v_{inf-sup}$ plotted as a function of h. (a) Results for the test in two dimensions, for which $\Omega = [0, 1]^2$. (b) Results for the test in three dimensions, for which $\Omega = [0, 1]^3$.

The results of the inf-sup test are given in Fig. 14. A sequence of nodal distributions of decreasing h is considered, in both two and three dimensions. The same behavior can be observed: The inf-sup values remain, for all practical purposes, essentially constant. Indeed, they exhibit a very small increase when h decreases: a linear regression applied to the graphs in Fig. 14 reveals that the dependence of $v_{inf-sup}$ on h assumes the approximate form $v_{inf-sup}(h) = C_1 h^{-0.0007}$ in the 2D case, and $v_{inf-sup} = C_2 h^{-0.0020}$ in the 3D case, where C_1 and C_2 are positive constants.

Hence we conclude that as h decreases, the inf-sup values do not approach zero, and (A.12) is satisfied. We say therefore that the meshfree spaces $\mathbb{V}_h[\mathbb{R}]$ and $\mathbb{P}_h[\mathbb{R}]$ form a compatible pair, which, using also other arguments, implies the stability of the mixed formulation (37).

References

[1] Bathe KJ. The finite element method with 'overlapping finite elements. In: Proceedings of the Sixth international conference on structural engineering, mechanics and computation – SEMC 2016, Cape Town, South Africa.
[2] Bathe KJ, Zhang L. The finite element method with overlapping elements – a new paradigm for CAD driven simulations. Comput Struct 2017;182:526–39.
[3] Zhang L, Bathe KJ. Overlapping finite elements for a new paradigm of solution. Comput Struct 2016 [submitted for publication].
[4] Strouboulis T, Copps K, Babuska I. The generalized finite element method. Comput Methods Appl Mech Eng 2001;190:4108–13.
[5] Melenk JM, Babuska I. The partition of unity finite element method: basic theory and applications. Comput Methods Appl Mech Eng 1996;139:289–314.
[6] Monaghan JJ. An introduction to SPH. Comput Phys Commun 1988;48:89–96.
[7] Belytschko T, Lu YY, Gu L. Element-free Galerkin methods. Int J Numer Meth Eng 1994;37:229–56.
[8] Zhu T, Zhang JD, Atluri SA. A local boundary integral equation (LBIE) method in computational mechanics, and a meshless discretization approach. Comput Mech 1998;21:223–35.
[9] Zhu T, Zhang JD, Atluri SA. A meshless local boundary integral equation (LBIE) method for solving nonlinear problems. Comput Mech 1998;22:174–86.
[10] De S, Bathe KJ. The method of finite spheres. Comput Mech 2000;25:329–45.
[11] Hong JW, Bathe KJ. Coupling and enrichment schemes for finite element and finite sphere discretizations. Comput Struct 2005;83:1386–95.
[12] Atluri S, Shen S. The meshless local Petrov-Galerkin method: a simple and less-costly alternative to the finite-element and boundary element methods. CMES: Comput Model Eng Sci 2002;3:11–51.
[13] Liu GR. Meshfree methods: moving beyond the finite element method. 2nd ed. CRC Press; 2010.
[14] Li S, Liu WK. Meshfree particle methods. Springer; 2007.
[15] Wu CT, Koishi M. Three-dimensional meshfree-enriched finite element formulation for micromechanical hyperelastic modeling of particulate rubber composites. Int J Numer Meth Eng 2012;91:1137–57.
[16] Simkins DC. Applications of meshfree methods in explicit fracture and medical modeling. In: Li S, Qian D, editors. Multiscale simulations and mechanics of biological materials. John Wiley & Sons; 2013.
[17] Li B, Stalzer M, Ortiz M. A massively parallel implementation of the optimal transportation meshfree method for explicit solid dynamics. Int J Numer Meth Eng 2014;100:40–61.
[18] Khoshghalb A, Khalili N. An alternative approach for quasi-static large deformation analysis of saturated porous media using meshfree method. Int J Numer Anal Meth Geomech 2015;39:913–36.
[19] Peco C, Millán D, Rosolen A, Arroyo M. Efficient implementation of Galerkin meshfree methods for large-scale problems with an emphasis on maximum entropy approximants. Comput Struct 2015;150:52–62.
[20] Ganzenmüller GC, Hiermaier S, May M. On the similarity of meshless discretizations of Peridynamics and Smooth-Particle Hydrodynamics. Comput Struct 2015;150:71–8.
[21] Roth MJ, Chen JS, Danielson KT, Slawson TR. Hydrodynamic meshfree method for high-rate solid dynamics using a Rankine-Hugoniot enhancement in a Riemann-SCNI framework. Int J Numer Meth Eng 2016.
[22] Cingoski V, Miyamoto N, Yamashita H. Element-free Galerkin method for electromagnetic field computations. IEEE Trans Magn 1998;34:3236–9.
[23] Maréchal Y. Some meshless methods for electromagnetic field computations. IEEE Trans Magn 1998;34:3351–4.
[24] Viana SA, Mesquita RC. Moving least squares reproducing kernel method for electromagnetic field computation. IEEE Trans Magn 1999;35:1372–5.
[25] Proekt L, Tsukerman I. Method of overlapping patches for electromagnetic computation. IEEE Trans Magn 2002;38:741–4.

[26] Yu Y, Chen Z. A 3-D radial point interpolation method for meshless time-domain modeling. IEEE Trans Microw Theory Tech 2009;57:2015–20.
[27] He Z, Chen RS. A vector meshless parabolic equation method for three-dimensional electromagnetic scatterings. IEEE Trans Antennas Propag 2015;63:2595–603.
[28] Yang S, Chen Z, Yu Y, Ponomarenko S. A divergence-free meshless method based on the vector basis function for transient electromagnetic analysis. IEEE Trans Microw Theory Tech 2014;62:1409–16.
[29] Yu Y, Chen Z. Towards the development of an unconditionally stable time-domain meshless method. IEEE Trans Microw Theory Tech 2010;58:578–86.
[30] Parreira G, Silva E, Fonseca A, Mesquita R. The element free Galerkin method in three-dimensional electromagnetic problems. IEEE Trans Magn 2006;42:711–4.
[31] Bottauscio O, Chiampi M, Manzin A. Element-free Galerkin method in eddy-current problems with ferromagnetic media. IEEE Trans Magn 2006;42:1577–84.
[32] Manzin A, Bottauscio O. Element-free Galerkin method for the analysis of electromagnetic-wave scattering. IEEE Trans Magn 2008;44:1366–9.
[33] Resende UC, Coppoli EHR, Afonso MM. A meshless approach using EFG interpolating moving least squares method in 2-D electromagnetic scattering analysis. IEEE Trans Magn 2015;51:1–4.
[34] Nicomedes W, Mesquita RC, Moreira FJS. A meshless local Petrov-Galerkin method for three dimensional scalar problems. IEEE Trans Magn 2011;47:1214–7.
[35] Nicomedes W, Mesquita RC, Moreira FJS. Calculating the band structure of photonic crystals through the meshless local Petrov-Galerkin (MLPG) method and periodic shape functions. IEEE Trans Magn 2012;48:551–4.
[36] Nicomedes W, Mesquita RC, Moreira FJS. The meshless local Petrov-Galerkin method in two-dimensional electromagnetic wave analysis. IEEE Trans Antennas Propag 2012;60:1957–68.
[37] Soares RD, Moreira FJS, Mesquita RC, Lowther DA, Lima NZ. A modified meshless local Petrov-Galerkin applied to electromagnetic axisymmetric problems. IEEE Trans Magn 2014;50:1–4.
[38] Wang LF. A parametric convex meshfree formulation for approximating the Helmholtz solution in circular coaxial waveguide. Int J Numer Model Electron Networks Devices Fields 2015;28:551–61.
[39] Nicomedes W, Mesquita RC, Moreira FJS. Meshless local Petrov-Galerkin (MLPG) methods in quantum mechanics. COMPEL (Bradford): Int J Comput Math Electr Electron Eng 2011;30:1763–76.
[40] Lu C, Shanker B. Generalized finite element method for vector electromagnetic problems. IEEE Trans Antennas Propag 2007;55:1369–81.
[41] Ern A, Guermond JL. Theory and Practice of Finite Elements. Applied Mathematical Sciences Series, Book 159. Springer; 2004.
[42] Monk P. Finite element methods for Maxwell's equations. Numerical mathematics and scientific computation series. Oxford University Press; 2003.
[43] Peterson AF, Ray SL, Mittra R. Computational methods for electromagnetics. IEEE Press Series on Electromagnetic Waves; 1998.
[44] Jin J. The finite element method in electromagnetics. 3rd ed. Wiley-IEEE Press; 2014.
[45] Embar A, Dolbow J, Harari I. Imposing Dirichlet boundary conditions with Nitsche's method and spline-based finite elements. Int J Numer Meth Eng 2010;83:877–98.
[46] Bathe KJ, Zhang H, Yan Y. The solution of Maxwell's equations in multiphysics. Comput Struct 2014;132:99–112.
[47] Girault V, Raviart PA. Finite element methods for Navier-Stokes equations – theory and algorithms. Springer series in computational mathematics, vol. 5. Springer; 1986.
[48] Bathe KJ. Finite element procedures. Prentice Hall; 1996. 2nd Edition, K. J. Bathe, Watertown, MA, 2014.
[49] Brezzi F, Fortin M. Mixed and hybrid finite elements. Springer series in computational mathematics, vol. 15. Springer; 1991.
[50] De S, Bathe KJ. Displacement/pressure mixed interpolation in the method of finite spheres. Int J Numer Meth Eng 2001;51:275–92.
[51] Balanis CA. Advanced engineering electromagnetics. 2nd ed. Wiley; 2012.
[52] Ham S, Bathe KJ. A finite element method enriched for wave propagation problems. Comput Struct 2012;94:1–12.
[53] Brezis H. Functional analysis, Sobolev spaces and partial differential equations. Springer Universitext, Springer; 2010.
[54] Ciarlet PG. Linear and nonlinear functional analysis with applications. Society for Industrial and Applied Mathematics – SIAM; 2013.
[55] Chapelle D, Bathe KJ. The finite element analysis of shells – fundamentals. Springer computational solid and fluid mechanics series. Springer; 2011.
[56] Quarteroni A. Numerical models for differential problems. MS&A: modeling, simulation & applications, vol. 2. Springer; 2009.
[57] Boffi D, Brezzi F, Fortin M. Mixed finite element methods and applications. Springer series in computational mathematics, vol. 44. Springer; 2013.
[58] Quarteroni A, Valli A. Numerical approximation of partial differential equations. Springer series in computational mathematics, vol. 23. Springer; 1994.
[59] Boyer F, Fabrie P. Mathematical tools for the study of the incompressible navier-stokes equations and related models. Applied mathematical sciences series, vol. 183. Springer; 2012.
[60] Harrington RF. Time-harmonic electromagnetic fields. 2nd ed. Wiley-IEEE Press; 2001.
[61] Boffi D. Finite element approximation of eigenvalue problems. Acta Numer 2010;19:1–120.
[62] Balanis CA. Antenna theory: analysis and design. 4th ed. Wiley; 2016.
[63] Akhmanov SA, Nikitin SYu. Physical optics. Clarendon Press; 1997.
[64] Heldring A, Rius JM, Ligthart L. New block ILU preconditioner scheme for numerical analysis of very large electromagnetic problems. IEEE Trans Magn 2002;38:337–40.
[65] Brezzi F, Bathe KJ. A discourse on the stability conditions for mixed finite element formulations. Comput Methods Appl Mech Eng 1990;82:27–57.
[66] Chapelle D, Bathe KJ. The inf-sup test. Comput Struct 1993;47:537–45.
[67] Iosilevich A, Bathe KJ, Brezzi F. On evaluating the inf-sup condition for plate bending elements. Int J Numer Meth Eng 1997;40:3639–63.
[68] Bathe KJ, Iosilevich A, Chapelle D. An inf-sup test for shell finite elements. Comput Struct 2000;75:439–56.
[69] Bathe KJ, Hendriana D, Brezzi F, Sangalli G. Inf-sup testing of upwind methods. Int J Numer Meth Eng 2000;48:745–60.
[70] Bathe KJ. The inf-sup condition and its evaluation for mixed finite elements. Comput Struct 2001;79:243–52.